Forward Generation of the GW150914 Gravitational-Wave Signal from a Constrained Propagation Model

Andrew Dodge
Auburn, Washington, USA

Version 1.0.3 - October 2025

Abstract

This work tests whether a source–observer propagation relation calibrated independently from Pantheon+ Type Ia supernova data can forward-generate the GW150914 gravitational-wave (GW) chirp when applied unchanged in the gravitational-wave domain. Using leading-order chirp dynamics recovered as the GR 0PN limit of the UMH formulation, together with this fixed propagation mapping, a strictly constrained forward waveform generator produces a waveform consistent with the observed inspiral–merger–ringdown morphology of GW150914, including chirp frequency evolution, merger timing, and a ringdown phase modeled as intrinsic relaxation dynamics.

The generated signal is projected onto the LIGO detectors using standard antenna response functions and geometric time delays. A separate comparison with the publicly available strain data uses a single global time/polarity registration anchor and introduces no per-detector fitting, phase adjustment, frequency remapping, empirical amplitude fitting, waveform reparameterization, or higher-order tuning.

This is not a template-fitting analysis, nor is it a competing replacement for General Relativity. In the present framing, the GR-order chirp law is recovered as the effective large-scale limit, while the specific objective of this paper is narrower: to test whether a propagation law fixed independently in cosmology remains self-consistent when applied to gravitational-wave observations. The propagation parameter governing the source–observer mapping is determined entirely from the Pantheon+ supernova dataset and is not recalibrated for the gravitational-wave signal, allowing GW150914 to serve as an independent cross-domain test.

The forward model reproduces key features of the observed GW150914 morphology without event-specific waveform tuning, yielding network signal-to-noise ratio (SNR) $\gtrsim 22$ at the strongest detector-network consistency point of the coarse event-configuration sweep, under standard whitening and fixed-registration diagnostics. These results demonstrate that a gravitational-wave chirp can be forward-generated from an independently calibrated propagation law while preserving consistency across frequency evolution, phase accumulation, amplitude normalization, and ringdown relaxation.

Position Statement

Critical Framing:

This paper should be read with one framing in mind. UMH is a proposed mechanical substrate (See Appendix D), from which **General Relativity and its quadrupole radiation law are recovered as the effective large-scale limit**.

Consequently, the leading-order (0PN) chirp relation used throughout is treated as the GR-order limit recovered from the UMH dynamics, not as a separate GR waveform model running in parallel. See Fig. 1 for the explanatory diagram and Secs. 2.3–2.5 for the derivation of the leading-order 0PN-equivalent chirp relation. This is **NOT** a replacement for General Relativity; GR is recovered as the effective limit used here.

The present work tests a single consequence of this framework: whether the **source–observer propagation mapping, calibrated independently on Pantheon+ supernovae and applied unchanged**, remains consistent in the gravitational-wave domain. (See Figure 2).

1 Introduction

Existing gravitational-wave pipelines perform parameter inference by matching observed data to large template banks. The present work addresses a different question: whether a specific gravitational-wave event can be forward-generated[1] from fixed physical assumptions prior to comparison with detector data.

1.1 Motivation

Gravitational-wave (GW) observations provide some of the most direct and high-precision tests of strong-field physics available. Events such as GW150914 capture the full evolution of a binary system — from slow inspiral through rapid chirping to post-merger ringdown — and therefore probe the underlying mechanism responsible for gravitational radiation across multiple dynamical regimes. In General Relativity (GR), these signals are modeled as perturbations of the spacetime metric, with waveform templates[12] constructed from a combination of post-Newtonian expansions, effective-one-body dynamics, and phenomenological fits calibrated to numerical relativity [7, 8, 9].

(Gravitational-wave) GW-pipeline waveforms incorporate post-Newtonian (PN) expansions together with additional corrections to capture the detailed evolution of compact-binary systems and their observational mapping. In the UMH framework, propagation effects such as redshift and time-dilation are encoded through a source–observer mapping that determines frequency evolution, phase accumulation, and amplitude scaling of the signal.

The propagation relation used in this work is derived within the ***Ultronic Medium Hypothesis (UMH)[1]***, where it is calibrated independently using cosmological observations. In the present analysis, this source–observer mapping is fixed a priori by Pantheon+ calibration[2] and is not fitted, adjusted, or re-optimized in the gravitational-wave domain. The full derivation is not required for this test and is provided in Appendix D.

Testing whether a propagation law calibrated from cosmological observations also reproduces compact-binary merger signals provides a direct empirical cross-domain test of the framework. In this context, GW150914 serves as a well-characterized test case for evaluating whether the same mapping generates binary-merger chirps consistent with observed data without phenomenological adjustment.

The GW150914 event provides a particularly well-characterized test case due to its high signal-to-noise ratio, clearly resolved inspiral–merger–ringdown structure, and the availability of well-studied reference data from the LIGO Hanford and Livingston detectors. This study investigates whether UMH can reproduce the full morphology of this event — instantaneous frequency evolution [10], amplitude growth, merger timing, and ringdown — using the model dynamics together with fixed source parameters and standard detector geometry.

Because the propagation mapping is fixed by cosmological calibration, it is not treated as a free parameter in the gravitational-wave analysis, and the prediction introduces no additional tuning beyond the physical binary configuration and standard detector geometry. The combination of fixed propagation, absence of waveform-level tuning, and cross-detector projection reduces the effective degrees of freedom such that reproducing the observed waveform is not generically achievable without the specific model structure.

---

[1] In this context, "forward generation" means the waveform is produced entirely from the UMH dynamical model prior to comparison with LIGO data, and the waveform shape is not modified during evaluation.

Figure 1: The **GR-order chirp law** is a node *downstream* of UMH dynamics — recovered as the large-scale limit, never imported as separate physics.

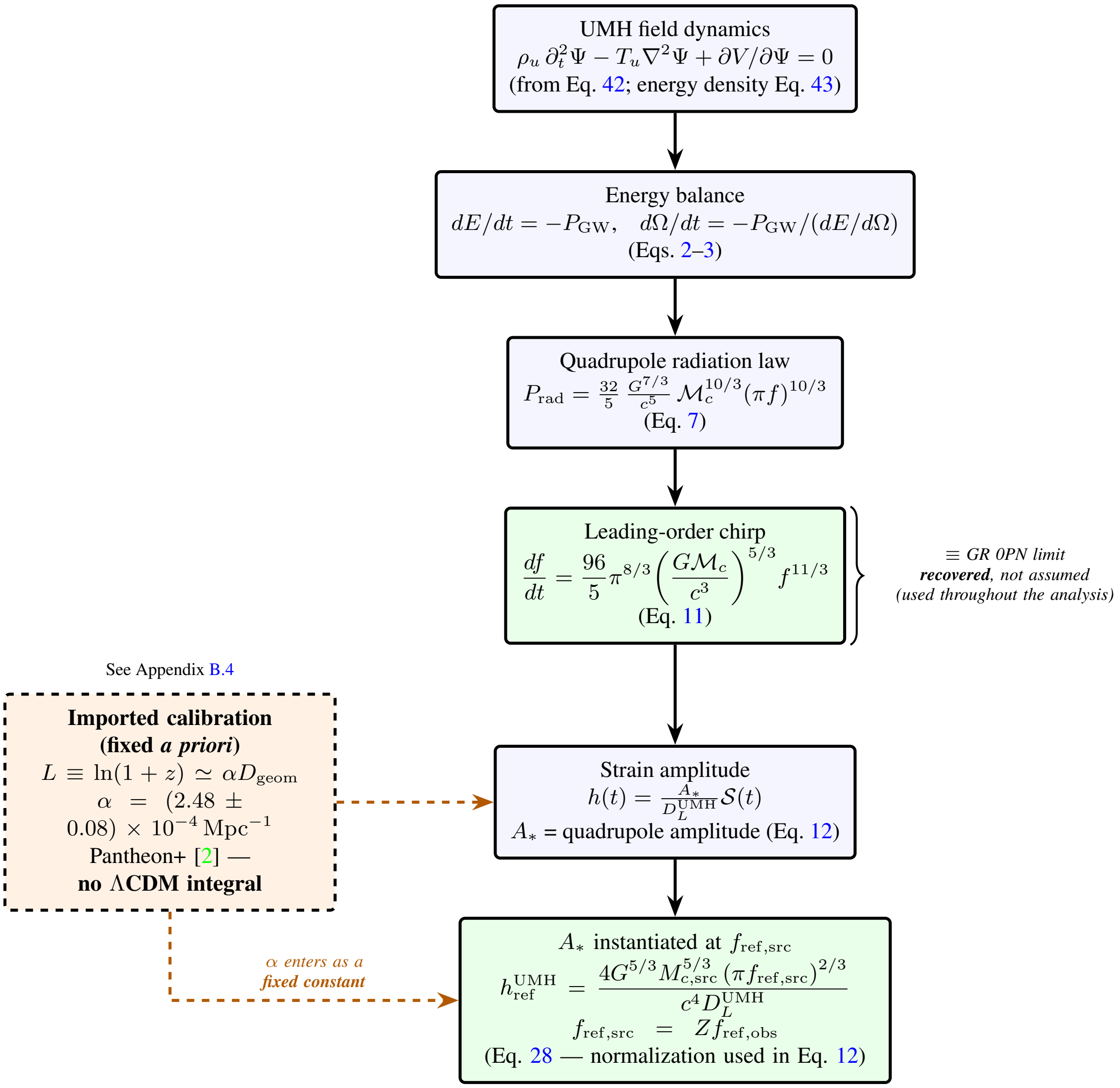

Figure 2: **Frequency, phase, and amplitude** are *not* adjusted independently — one calibrated operator Z maps all three from source to observer. This is the source–observer consistency being tested.

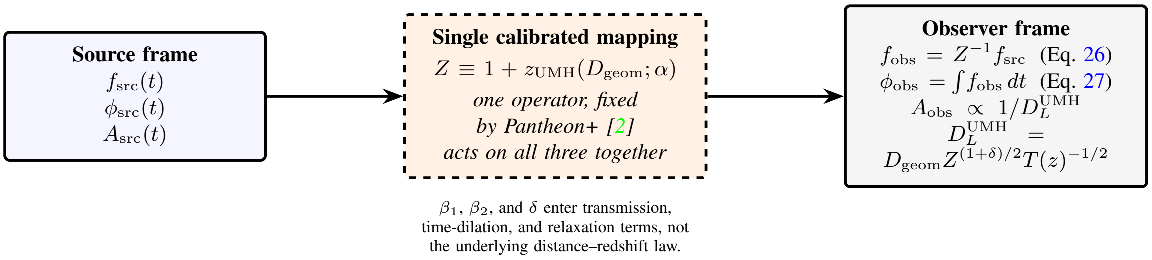

In the UMH test performed here, the Pantheon+-calibrated source–observer operator Z is applied explicitly before comparison, so distance, observer-frame frequency evolution, phase accumulation, and amplitude normalization are determined together by the same mapping. This is the consistency being tested. In standard detector-frame analyses, by contrast, the redshift contribution to frequency and phase is represented through the recovered detector-frame mass scale, with source-frame quantities assigned afterward through an assumed distance–redshift relation. See Sec. 5.2.2.

1.2 Objectives of this Paper

The primary objective of this paper is to evaluate whether a forward generator can reproduce the full gravitational-wave morphology of the GW150914 event using only a fully specified, constraint-based formulation, without relying on post-Newtonian parameter tuning or phenomenological template fitting. We seek to determine whether a chirp generated from UMH-derived relations — using a single intrinsic waveform, a tension-based amplitude law, detector geometry alone, and a propagation parameter fixed independently by the Pantheon+ supernova calibration — can reproduce the principal observed waveform features consistent with those recovered in standard GW analyses when compared to LIGO observational data.

To this end, we employ two independent pipelines: a dedicated UMH chirp generator that produces the intrinsic inspiral–merger–ringdown waveform from the model formulation, and a strictly separated UMH–Detector comparison pipeline that applies only physical registration (using a single global time and polarity registration, fixed across detectors), whitening, and detector-response operations. This separation ensures that the comparison remains unbiased and that no shared implementation artifacts influence the results. (See flow chart Fig. 3 for reference.)

The analysis focuses on several key performance metrics:

(i) Agreement between the UMH instantaneous frequency evolution and the Hilbert-transform-derived frequency track from LIGO data,
(ii) Consistency of merger timing, amplitude growth, and ringdown frequency across detectors,
(iii) Whitened time-domain overlap and correlation within the merger window, and
(iv) Spectrogram and amplitude–spectral–density comparisons evaluated under a fixed, constraint-enforced registration.

The goal is not merely to match the observed signal, but to test whether the UMH forward-generation framework reproduces the observed GW150914 morphology under fixed propagation and registration constraints.

By demonstrating that UMH yields a clean, physically justified chirp that agrees closely with LIGO observations, this work aims to establish gravitational-wave measurements as an independent observational domain — alongside cosmology, in which the UMH propagation law was originally calibrated — in which the UMH framework can be tested against empirical data and evaluated as a constrained forward-generation description of gravitational-wave signals.

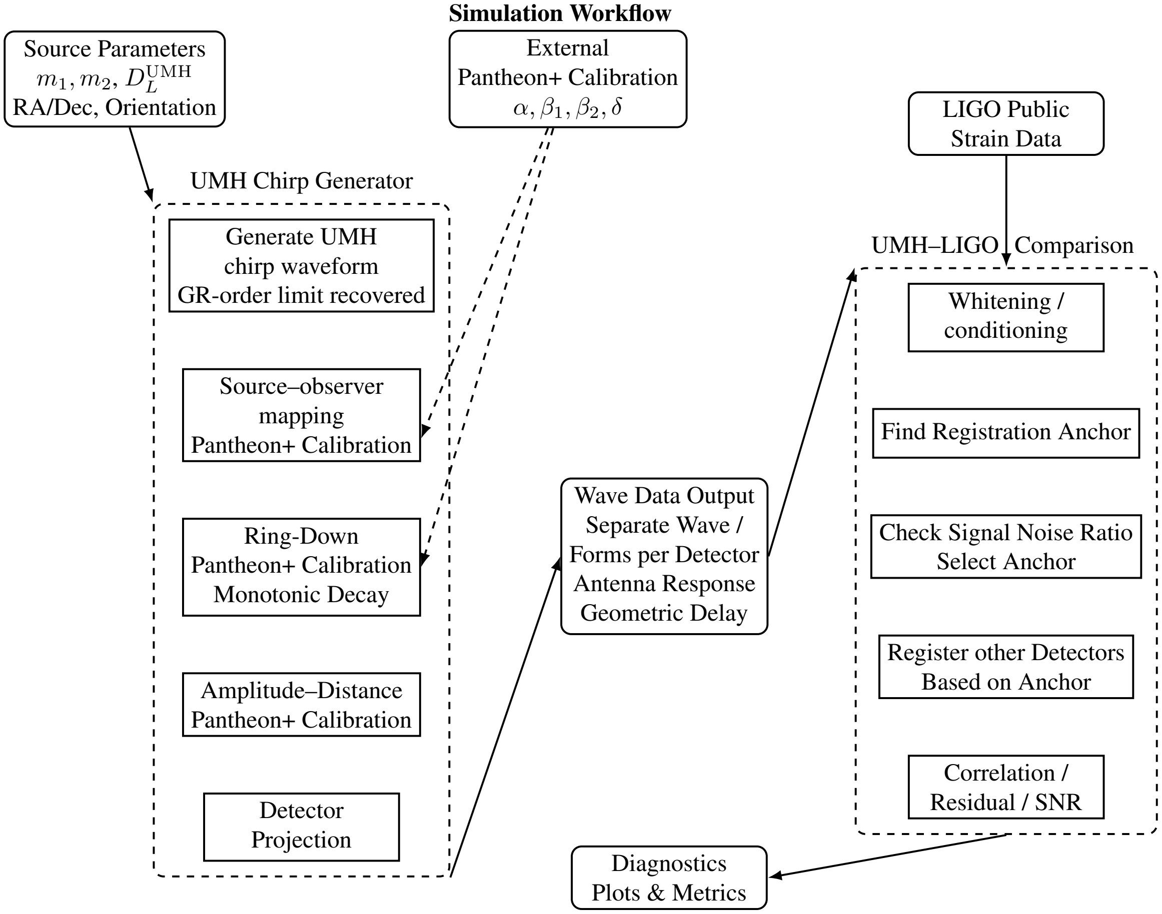

Figure 3: **Simulation Workflow** of the UMH forward-generation and comparison pipeline. The chirp generator operates independently of detector data, producing the intrinsic waveform prior to comparison with LIGO strain.

2 UMH Chirp Theory

2.1 Overview of UMH-Based Waveform Construction

The waveform generation used in this work is based on a propagation framework derived within the ***Ultronic Medium Hypothesis (UMH)****[1]*, which models gravitational-wave signals as propagating strain disturbances. In the present analysis, only the resulting propagation mapping and leading-order waveform evolution are required; the full field formulation and medium-level derivation are provided in Appendix D.

Operationally, the model consists of (i) a leading-order inspiral evolution consistent with standard quadrupole scaling, and (ii) a source–observer mapping that governs amplitude normalization, frequency evolution, phase accumulation, and time dilation. This mapping is calibrated independently using the Pantheon+ dataset and is applied unchanged in the gravitational-wave domain.

This formulation yields a forward-generated waveform in which propagation effects are coupled across observables rather than treated as independent adjustments, providing the operational basis for the chirp-generation model evaluated in the present analysis.

2.2 Orbital Evolution in UMH

Binary orbital energy is radiated through propagating strain disturbances in the model. The radiated power corresponds to the outward flux of the wave-energy density defined in Eq. (43),

$$\frac{dE}{dt} = -\oint \mathbf{F}_\Psi \cdot d\mathbf{A}, \tag{1}$$

where $\mathbf{F}_\Psi$ denotes the energy-flux vector associated with the propagating strain perturbation Ψ.
The resulting radiated power determines the orbital energy loss that drives the inspiral evolution used in Eq. (2).
The inspiral is governed by the coupling between the binary's changing quadrupolar configuration and the model's energy-transfer formulation.

$$\frac{dE}{dt} = -\mathcal{P}_{\rm GW}(t), \tag{2}$$

where $\mathcal{P}_{\rm GW}$ is the instantaneous strain-energy flux carried away by the propagating strain field.
The orbital frequency evolves according to

$$\frac{d\Omega}{dt} = -\frac{\mathcal{P}_{\rm GW}}{dE/d\Omega}, \tag{3}$$

which has the same structural form as the leading-order inspiral relation obtained in General Relativity and is consistent with the standard energy-balance description of binary inspiral. In the present formulation, the proportionality constant depends on the coupling strength between the binary quadrupole moment and the surrounding strain field. In the weak-field regime, this reduces to the familiar Newtonian hardening. Within the broader framework, General Relativity is recovered as an effective large-scale description of the underlying dynamics.

For a compact binary in quasi-circular orbit, the orbital energy depends on the orbital frequency through the Newtonian relation

$$E(\Omega) \propto -\Omega^{2/3}, \tag{4}$$

which follows from the Keplerian scaling between orbital separation and frequency.

Substituting the Newtonian energy relation into Eq. (3) yields the characteristic inspiral scaling

$$\frac{d\Omega}{dt} \propto \Omega^{11/3}, \tag{5}$$

which produces the rising-frequency "chirp" behavior observed in gravitational-wave signals. The explicit coefficient governing this evolution is derived in the next subsection.

The inspiral accelerates as orbital separation decreases, producing the characteristic "chirp" of rising frequency and amplitude. This behavior follows directly from the energy-transfer formulation used in the model formulation without requiring perturbative post-Newtonian expansions in this implementation.

2.3 UMH Derivation of the Leading Chirp Evolution

The explicit coefficient governing the inspiral chirp evolution follows from energy balance between orbital binding energy and radiative power carried by propagating strain waves as defined in the model.
For a quasi-circular binary the Newtonian binding energy is

$$E_{\rm orb} = -\frac{Gm_1m_2}{2r}. \tag{6}$$

The radiative power emitted in the recovered far-field transverse–traceless sector of the UMH framework is taken from the full UMH radiation-sector derivation in Ref. [1] and summarized in Appendix C, giving the leading-order quadrupole radiation law,

$$P_{\rm rad} = \frac{32}{5}\frac{G^{7/3}}{c^5}M_c^{10/3}(\pi f)^{10/3}. \tag{7}$$

Energy balance requires

$$\frac{dE_{\rm orb}}{dt} = -P_{\rm rad}. \tag{8}$$

Using Kepler's relation

$$\Omega^2 = \frac{G(m_1+m_2)}{r^3} \tag{9}$$

and identifying the gravitational-wave frequency

$$f = \frac{\Omega}{\pi}, \tag{10}$$

one obtains the frequency evolution.

Substituting Eq. (7) into the energy-balance relation (8) and applying the Keplerian relation (9) yields the frequency evolution given in Eq. (11).

$$\frac{df}{dt} = \frac{96}{5}\pi^{8/3}\left(\frac{GM_c}{c^3}\right)^{5/3} f^{11/3}. \tag{11}$$

This is the leading-order inspiral chirp equation (0PN-equivalent), consistent with the standard quadrupole prediction of General Relativity, which is therefore recovered as the effective large-scale limit of the formulation.

In the present formulation, the radiative power reduces to the standard quadrupole form in the weak-field limit, yielding the normalization coefficient $32/5$, consistent with leading-order gravitational-wave emission.

2.4 UMH Strain Equation

In UMH, the observed strain amplitude is normalized by the same effective luminosity-distance mapping used in the Pantheon+ calibration:

$$h(t) = \frac{A_*}{D_L^{\rm UMH}}\,\mathcal{S}(t), \tag{12}$$

where A_* is the intrinsic source amplitude scale determined by the binary parameters, $\mathcal{S}(t)$ is the intrinsic strain function generated by the inspiral dynamics of the model, and $D_L^{\rm UMH}$ is the UMH effective luminosity distance defined in Eq. 24. The redshift, time-dilation, and transmission factors entering the amplitude normalization are therefore contained in $D_L^{\rm UMH}$ and are not applied a second time as an additional multiplicative factor. Because this source–observer mapping is calibrated once using the Pantheon+ supernova dataset, it fixes the amplitude normalization used throughout the model. The same calibration determines the associated frequency evolution, phase accumulation, and relativistic time dilation without introducing additional adjustable degrees of freedom.

The Pantheon+ calibration therefore fixes the global source–observer mapping used in the UMH framework; the binary source parameters remain event-level inputs, and no event-specific recalibration is performed in the gravitational-wave analysis. In the companion Pantheon+ analysis [2], the UMH source–observer mapping is calibrated from the Pantheon+ low-redshift sample using the logarithmic geometric-distance relation $L \equiv \ln(1+z) \simeq \alpha D_{\rm geom}$, yielding $\alpha = (2.48\pm0.08)\times10^{-4}\,{\rm Mpc}^{-1}$ for the Pantheon+ Type Ia supernova sample.

In the present gravitational-wave analysis, this same calibrated propagation scale is applied unchanged to the UMH source–observer mapping governing amplitude normalization, frequency redshift, phase accumulation, and time dilation.

$$L \equiv \ln(1+z) \simeq \alpha D_{\rm geom}. \tag{13}$$

2.5 UMH Frequency Evolution

The gravitational-wave frequency in UMH is twice the orbital frequency:

$$f_{\mathrm{GW}}(t) = \frac{\Omega(t)}{\pi}, \tag{14}$$

and evolves according to the model energy-loss law. The phase is obtained by integrating the instantaneous frequency:

$$\phi(t) = \phi_0 + 2\pi \int_{t_0}^{t} f_{\mathrm{GW}}(t')\, dt'. \tag{15}$$

Using the coefficient derived above, UMH yields a Newtonian-order analytic chirp evolution consistent with the leading-order inspiral scaling obtained in GR, but derived here from the model's energy-transfer formulation.

$$\frac{df_{\mathrm{GW}}}{dt} = K_{\mathrm{UMH}}\, f_{\mathrm{GW}}^{11/3}, \tag{16}$$

where K_{UMH} is the leading-order chirp coefficient.
The chirp mass is defined as

$$M_c = \frac{(m_1 m_2)^{3/5}}{(m_1 + m_2)^{1/5}}. \tag{17}$$

In the present implementation, this coefficient is given by

$$K_{\mathrm{UMH}} = \frac{96}{5}\, \pi^{8/3} \left(\frac{G\, M_{c,\mathrm{src}}}{c^3} \right)^{5/3}. \tag{18}$$

This coefficient corresponds to the leading-order (0PN-equivalent) inspiral evolution. Higher-order post-Newtonian corrections are not required for the present comparison because the dominant chirp morphology is already captured by the Newtonian-order evolution.

Integrating this relation gives the closed-form evolution

$$t_c - t = \frac{3}{8K_{\mathrm{UMH}}}\, f_{\mathrm{GW}}^{-8/3}, \qquad f_{\mathrm{GW}}(t) \propto (t_c - t)^{-3/8}. \tag{19}$$

The instantaneous frequency calculated from the analytic UMH law provides the frequency track later compared with the Hilbert-derived frequency extracted from LIGO data.

This analytic evolution provides the intrinsic frequency track used in the UMH chirp generator and forms the basis for the subsequent comparison with LIGO observations.

This coefficient corresponds exactly to the value implemented in the UMH chirp generator used for the forward waveform construction in the present analysis.

2.6 UMH Source–Observer Mapping Summary

For clarity, the Pantheon+-calibrated UMH propagation is implemented as a source–observer mapping applied within the waveform generator rather than a single closed-form expression. The mapping proceeds as follows.

The UMH propagation calibration defines an effective tension redshift through the geometric source–observer distance,

$$z_{\mathrm{UMH}} = z_{\mathrm{UMH}}(D_{\mathrm{geom}}; \alpha), \tag{20}$$

where α is the source–observer propagation scale fixed by the Pantheon+ low-redshift calibration. In the homogeneous calibration limit used here,

$$D_{\mathrm{geom}}(z) = \frac{\ln(1+z)}{\alpha}. \tag{21}$$

The corresponding source–observer redshift factor is

$$Z \equiv 1 + z_{\mathrm{UMH}}. \tag{22}$$

The event-distance values listed in the source-parameter tables are not inserted directly into Eq. 20 as D_{geom}. They are the UMH effective luminosity distances D_L^{UMH} used as event-level source-distance inputs. The geometric distance entering the redshift law is related to this tabulated distance through the same Pantheon+-calibrated luminosity/transmission mapping used in the supernova analysis,

$$T(z) = \exp\left[-\beta_1 \ln(1+z) - \beta_2 \ln^2(1+z)\right], \tag{23}$$

$$D_L^{\mathrm{UMH}}(z) = D_{\mathrm{geom}}(z)\,(1+z)^{(1+\delta)/2}\,T(z)^{-1/2}, \qquad \delta = 1. \tag{24}$$

Thus, for each gravitational-wave event, z_{UMH} is obtained by numerically inverting Eq. 24 for the tabulated D_L^{UMH}, and the corresponding D_{geom} is then obtained from Eq. 21. Equation 20 therefore applies to the geometric distance D_{geom}, not directly to the tabulated luminosity-distance column.

This redshift factor determines the source-frame to observer-frame frequency and phase mapping. The remaining Pantheon+-calibrated quantities used in the present generator enter through the transmission, amplitude-normalization, and relaxation mappings, not through the underlying distance–redshift law. The fixed Pantheon+-calibrated transmission coefficients enter the post-merger relaxation mapping through

$$\beta_{\mathrm{eff}}(z_{\mathrm{UMH}}) = \beta_1 + 2\beta_2 \ln(1 + z_{\mathrm{UMH}}), \tag{25}$$

which is evaluated using the redshift determined above. Thus β_1 and β_2 modify the transmission and relaxation response, not the distance–redshift law itself.

This mapping determines the transformation from source-frame to observer-frame quantities. The observed gravitational-wave frequency evolves as

$$f_{\mathrm{obs}}(t) = Z^{-1} f_{\mathrm{src}}(t), \tag{26}$$

with phase obtained by integration,

$$\phi_{\mathrm{obs}}(t) = \phi_0 + 2\pi \int_{t_0}^{t} f_{\mathrm{obs}}(t')\,dt'. \tag{27}$$

Amplitude normalization is fixed globally by the UMH quadrupole scaling at a reference frequency. The waveform arrays are sampled and compared in observer time, so the normalization point is selected at an observer-frame reference frequency $f_{\mathrm{ref,obs}}$. The quadrupole amplitude itself is evaluated using the corresponding source-frame frequency, $f_{\mathrm{ref,src}} = Z f_{\mathrm{ref,obs}}$, together with the source-frame chirp mass $M_{c,\mathrm{src}}$:

$$h_{\mathrm{ref}}^{\mathrm{UMH}} = \frac{4G^{5/3} M_{c,\mathrm{src}}^{5/3} \left(\pi f_{\mathrm{ref,src}}\right)^{2/3}}{c^4 D_L^{\mathrm{UMH}}}, \qquad f_{\mathrm{ref,src}} = Z f_{\mathrm{ref,obs}}. \tag{28}$$

This defines a single global amplitude factor G_{amp} applied to the generated waveform without detector-specific adjustment. Here D_L^{UMH} is the UMH effective luminosity distance defined in Eq. 24. Thus Eq. 28 is not an additional strain assumption; it is the reference-frequency amplitude normalization corresponding to the strain form in Eq. 12. The source–observer redshift, time-dilation, and transmission factors enter the amplitude once through D_L^{UMH}, so no additional D_{eff} factor or separate $(1 + z_{\mathrm{UMH}})^{-1}$ amplitude factor is applied.

The observed strain in detector d is then given by

$$\begin{aligned} h_d(t) = {} & F_{+,d}\, A_{\mathrm{obs}}(t - \tau_d) \frac{1 + \cos^2 \iota}{2} \cos\big(\phi_{\mathrm{obs}}(t - \tau_d)\big) \\ & + F_{\times,d}\, A_{\mathrm{obs}}(t - \tau_d) \cos\iota \, \sin\big(\phi_{\mathrm{obs}}(t - \tau_d)\big), \end{aligned} \tag{29}$$

where $F_{+,d}$ and $F_{\times,d}$ are the detector antenna response functions and τ_d is the geometric time delay.

This mapping is fixed by the Pantheon+-calibrated UMH propagation mapping and applied uniformly across all simulations without event-specific tuning, providing a direct forward-generation test of the UMH propagation framework.

2.7 Ringdown as a Damped Relaxation Process

Following merger, the post-merger phase is governed by the intrinsic relaxation dynamics of the strain field. In this regime, the governing wave equation admits a late-time damped oscillatory solution arising from energy dissipation and relaxation toward an equilibrium configuration of the remnant system, with the response determined by the intrinsic relaxation parameters of the model. (See diagram Figure 4 for an explanation of this process).

To leading order, the post-merger strain is therefore described by a damped relaxation response,

$$h_{\rm RD}(t) = A_{\rm RD}\, e^{-(t-t_m)/\tau_{\rm UMH}} \sin[\phi_{\rm RD}(t)]\,, \qquad t \geq t_m, \qquad \frac{d\phi_{\rm RD}}{dt} = 2\pi f(t). \tag{30}$$

where $A_{\rm RD}$ is the post-merger strain amplitude, t_m is the merger time, $\tau_{\rm UMH}$ is the characteristic damping time defined within the model, and $f(t)$ is the instantaneous post-merger frequency that relaxes toward the asymptotic post-merger frequency $f_{\rm RD}$ according to Eq. (34).

The quantities $f_{\rm RD}$ and $\tau_{\rm UMH}$ are not tuned to match detector data. In the current implementation, the progenitor component spins are set to zero, but the post-merger relaxation scale is evaluated using the derived remnant mass and final remnant spin associated with the nonprecessing binary configuration. The asymptotic relaxation frequency is initialized from the recovered GR-limit $(2, 2, 0)$ ringdown scale and is then propagated through the UMH source–observer mapping, while the subsequent frequency retuning is governed by the UMH medium-relaxation law and the fixed Pantheon+-calibrated transmission coefficient $\beta_{\rm eff}$.

For reproducibility, the GR-limit $(2, 2, 0)$ reference scale used to initialize the relaxation frequency is evaluated as

$$f_{220,\rm src} = \frac{c^3}{2\pi G M_f}\left[1.5251 - 1.1568(1-a_f)^{0.1292}\right], \qquad f_{220,\rm obs} = \frac{f_{220,\rm src}}{1+z_{\rm UMH}}, \tag{31}$$

where M_f and a_f are the remnant mass and dimensionless final remnant spin used by the generator.[2] For the baseline GW150914 run, the generator uses $M_{f,\rm src} = 68.941\, M_\odot$, $a_f = 0.686$, and $z_{\rm UMH} = 0.0790$, giving $f_{220,\rm src} = 248.024$ Hz and $f_{220,\rm obs} = 229.855$ Hz; for this run $f_{\rm RD} = f_{220}$, with no additional mapping between the $(2, 2, 0)$ reference frequency and the asymptotic ringdown frequency beyond the UMH source–observer redshift.[3]

The resulting relaxation frequencies are therefore fixed prior to comparison with detector data and should be interpreted as a constrained leading-order, nonprecessing-remnant relaxation approximation rather than as a precision remnant-spin or QNM-spectrum reconstruction. The present comparison is therefore interpreted as a constrained morphology and relaxation test, not as a precision remnant-spin or QNM-spectrum reconstruction. In the present formulation, this behavior is described through a damped UMH relaxation response rather than a fitted quasi-normal-mode (QNM) overtone decomposition. A detailed interpretation for the UMH framework used in this paper is provided in Sec. 2.8, Appendix D, and Ref. [1].

Accordingly, the UMH ringdown is interpreted as the physical dissipation and frequency retuning of strain energy following merger rather than as an event-fitted modal decomposition of spacetime perturbations. This interpretation naturally provides a description consistent with the observed damping behavior. (See Figs. 5 and 6).

This form captures the dominant post-merger relaxation behavior and provides the effective ringdown model used in the UMH chirp generator.

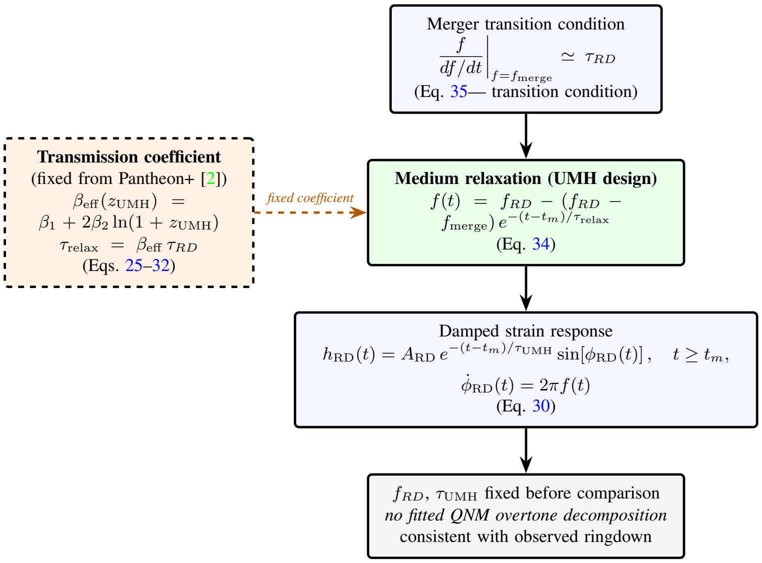

Figure 4: The **ringdown is modeled as a UMH medium-relaxation process**, not as a fitted quasi-normal-mode overtone decomposition. The asymptotic post-merger scale is fixed before comparison, while the frequency relaxation is governed by the UMH relaxation law together with the fixed Pantheon+-calibrated transmission coefficient. The amplitude envelope decays on the intrinsic medium timescale, and the full post-merger response is propagated through the same source–observer mapping.

---

[2] The remnant quantities M_f and a_f are computed deterministically from the source-frame component masses and spins using the nonprecessing SEOBNRv4 remnant final-mass/final-spin fit as implemented in LALSimulation; in the present runs the component spins are set to zero.

[3] The agreement with the Kerr ((2,2,0)) scale should be read as a GR-limit recovery of the UMH remnant construction, not as a detector-domain QNM fit or overtone-template attachment.

2.8 Relaxation and Frequency Retuning

Following merger the post-merger system is modeled as relaxing toward an equilibrium configuration corresponding to the remnant compact object. The oscillation frequency therefore approaches the ringdown frequency f_{RD} through a relaxation process defined within the model.

The effective relaxation timescale is determined by the effective transport parameters calibrated from the Pantheon+ supernova dataset. As introduced in Eq. 25, the effective medium transport parameter β_{eff} is evaluated as a function of the UMH tension redshift z_{UMH}. The characteristic frequency relaxation time is then

$$\tau_{\mathrm{relax}} = \beta_{\mathrm{eff}}\, \tau_{RD}, \tag{32}$$

where τ_{RD} is the intrinsic damping time of the model response in the source frame prior to the source–observer mapping.

In the present implementation, the source-frame damping time appearing in Eq. (30) is identified with the intrinsic medium ringdown timescale,

$$\tau_{\mathrm{UMH}} \equiv \tau_{RD}. \tag{33}$$

Equation (33) is an identification rather than a derived relation: τ_{RD} denotes the single intrinsic relaxation timescale of the post-merger medium response in the source frame, and Eq. (33) states that the amplitude envelope of Eq. (30) decays on this bare intrinsic timescale, without transport rescaling. The frequency relaxation, by contrast, proceeds on the transport-modified timescale $\tau_{\mathrm{relax}} = \beta_{\mathrm{eff}}\, \tau_{RD}$ (Eq. 32); the two processes therefore share the same intrinsic time τ_{RD} but differ by the medium transport factor β_{eff}, which governs frequency settling but not amplitude decay. The additional timescale τ_{relax} governs the relaxation of the instantaneous oscillation frequency toward f_{RD} and is therefore distinct from the amplitude damping time τ_{UMH}.

The intrinsic ringdown damping time is fixed by the UMH remnant damping-cycle rule,

$$\tau_{\mathrm{RD,src}} = \frac{N_{\mathrm{RD}}}{f_{\mathrm{RD,src}}}, \qquad N_{\mathrm{RD}} = 1.00.$$

Thus τ_{RD} is not adjusted using detector data and is not solved from the observed residual. The closure order is: the remnant configuration fixes $f_{\mathrm{RD,src}}$; the global UMH damping-cycle rule fixes $\tau_{\mathrm{RD,src}}$; Eq. (35) then determines the active inspiral–ringdown transition frequency f_{merge}. Observer-frame times are obtained by the same source–observer mapping used throughout the generator,

$$\tau_{\mathrm{RD,obs}} = Z\, \tau_{\mathrm{RD,src}}, \qquad \tau_{\mathrm{relax,src}} = \beta_{\mathrm{eff}}(z_{\mathrm{UMH}})\, \tau_{\mathrm{RD,src}}, \qquad \tau_{\mathrm{relax,obs}} = Z\, \tau_{\mathrm{relax,src}},$$

where $Z = 1 + z_{\mathrm{UMH}}$. This convention is fixed before comparison and is applied uniformly across detectors. See Table B.5 for event damping numbers.

The instantaneous post-merger frequency therefore relaxes toward the asymptotic ringdown frequency according to an exponential medium-response law,

$$f(t) = f_{RD} - (f_{RD} - f_{\mathrm{merge}}) \exp\left[-\frac{t - t_m}{\tau_{\mathrm{relax}}}\right], \qquad t \geq t_m, \tag{34}$$

where t_m denotes the merger time and f_{merge} is the frequency at the inspiral–ringdown transition.

Within the UMH generator, the inspiral–ringdown transition occurs when the inspiral driving timescale becomes comparable to the intrinsic medium relaxation timescale,

$$\left.\frac{f}{df/dt}\right|_{f=f_{\mathrm{merge}}} \simeq \tau_{RD}. \tag{35}$$

This condition determines the merger frequency f_{merge} used to anchor the onset of the post-merger relaxation phase. The ringdown frequency f_{RD} corresponds to the equilibrium oscillation frequency of the remnant configuration as defined in the model following merger. This transition corresponds physically to the point where the inspiral driving rate can no longer exceed the intrinsic relaxation rate of the system response defined within the model.

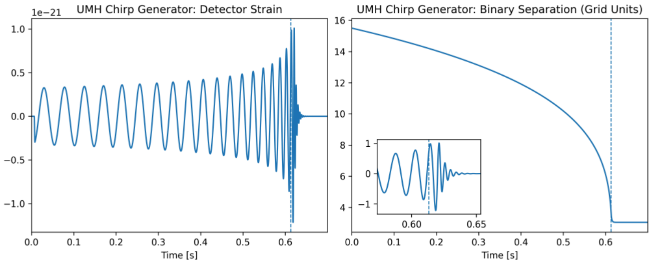

Figure 5: **Intrinsic UMH chirp dynamics Hanford:**
Left: UMH-generated detector strain, prior to any comparison with LIGO data, showing the accelerating chirp approaching merger.
Right: Binary separation in UMH grid units, illustrating the tension-driven inspiral responsible for the waveform's frequency and amplitude evolution.

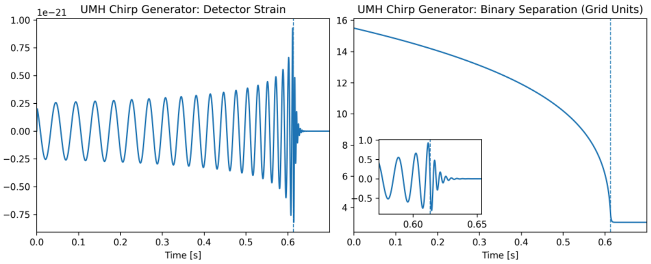

Figure 6: **Intrinsic UMH chirp dynamics Livingston:**
Left: UMH-generated detector strain, prior to any comparison with LIGO data, showing the accelerating chirp approaching merger.
Right: Binary separation in UMH grid units, illustrating the tension-driven inspiral responsible for the waveform's frequency and amplitude evolution.

No frequency rescaling, phase warping, or time reparameterization is applied beyond the fixed source–observer mapping determined by the Pantheon+-calibrated medium tension.

3 Methods

3.1 UMH Chirp Generation Pipeline

The intrinsic gravitational-wave signal used in this study is generated using a dedicated UMH chirp-production code (`UMH_Chirp_Generator.py`; see Appendix F). The generator implements the mechanical evolution of a binary system embedded in this model's formulation and produces a complete inspiral–merger–ringdown waveform directly from the mechanical evolution equations of the UMH framework.

The generator solves for the orbital decay, instantaneous frequency, amplitude growth, and final ringdown using only the physical parameters of the binary system (component masses, orbital configuration, and detector geometry) together with the mechanical energy-transfer laws in the present model. No post-Newtonian terms beyond the leading-order (0PN-equivalent) level are included, and no phenomenological corrections are introduced. All waveform features emerge from the mechanical hardening of the binary and its coupling to the medium, ensuring a direct and transparent connection between UMH theory and the resulting chirp. The component spins are set to zero in the present analysis, so no spin parameters enter the waveform generation.

To preserve methodological independence, the waveform generator is fully isolated from the comparison pipeline. The generator produces the intrinsic waveform before any interaction with detector data, ensuring that no information from the LIGO observations influences the predicted signal. It outputs:

(i) The intrinsic strain waveform for each polarization,
(ii) The analytic instantaneous frequency $f_{\mathrm{GW}}(t)$,
(iii) The UMH tension–redshift propagation correction applied to the strain amplitude, and
(iv) Metadata including chirp mass, merger frequency, ringdown parameters, and detector-independent timing.

This separation ensures that no information from the LIGO data influences the generated waveform prior to the comparison stage.

The source–observer propagation mapping used in the generator is fixed a priori by the Pantheon+ calibration described in Ref. [2] and is not treated as a free parameter in the gravitational-wave analysis.

The forward-generated waveform exhibits a coherent time–frequency evolution, as shown in Figs. 7 and 8, where the analytic frequency track $f_{\mathrm{GW}}(t)$ closely follows the spectrogram power ridge in both detectors.

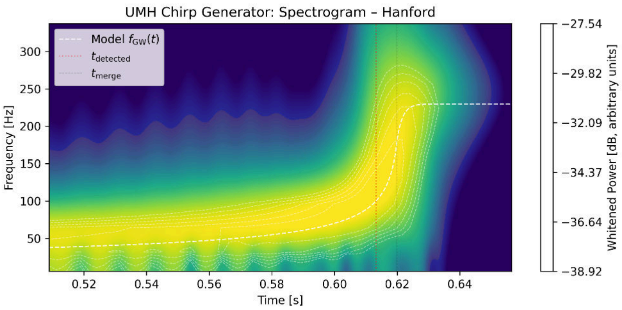

Figure 7: **UMH-generated spectrogram for the Hanford detector:** showing the frequency evolution and merger timing. The analytic UMH frequency track $f_{\mathrm{GW}}(t)$ (white dashed) closely follows the power ridge of the simulated signal.

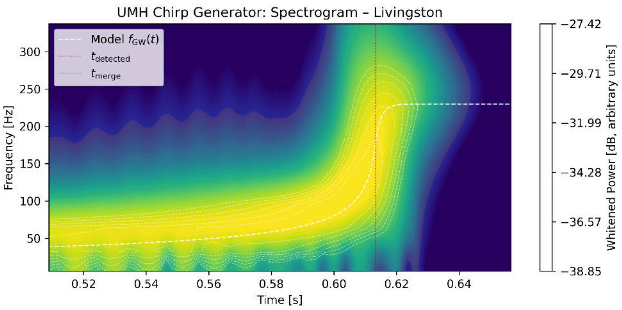

Figure 8: **UMH-generated spectrogram for the Livingston detector:** showing the frequency evolution and merger timing. The analytic UMH frequency track $f_{\mathrm{GW}}(t)$ (white dashed) closely follows the power ridge of the simulated signal.

3.1.1 Detector Geometry and Propagation

To compare the intrinsic UMH chirp with the gravitational-wave observations, the waveform is projected onto the active detector set for the event under study—Hanford and Livingston for GW150914, and Hanford, Livingston, and Virgo for GW170814—using the standard detector antenna response functions. The effective strain observed at detector D is given by:

$$h_D(t) = F_D^{+}(\theta,\phi,\psi)\, h_{+}(t-\Delta t_D) + F_D^{\times}(\theta,\phi,\psi)\, h_{\times}(t-\Delta t_D), \tag{36}$$

where $F_D^{+,\times}$ are the detector pattern functions, (θ, ϕ, ψ) denote the event-specific source sky location and polarization orientation, and Δt_D is the geometric arrival-time delay. The plus and cross polarizations h_{+} and $h_{\times}$ are intrinsic to the medium strain tensor rather than supplied by the antenna projection; their origin and the spin-2 character of the radiation are derived in Appendix C.

The time delay between Hanford and Livingston is computed directly from the source sky geometry. For GW150914 this geometry yields a delay of approximately $6.6\,\mathrm{ms}$, consistent with the delay measured in the LIGO observations.

Each detector receives the same intrinsic UMH waveform; the only differences arise from:

(i) Antenna pattern projection,

(ii) Geometric time delay, and

(iii) A single global amplitude scaling determined by the Pantheon+ supernova calibration of the UMH propagation law.

No per-detector tuning or empirical scaling is applied.

Diagnostic plots of the generated chirp and spectrogram are provided for each detector to illustrate the resulting signal structure and a representative Hanford diagnostic plot of the generated chirp instantaneous frequency is provided in Fig. 9.

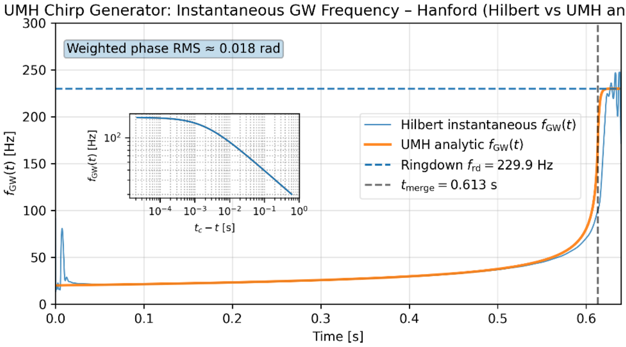

Figure 9: **Instantaneous gravitational-wave frequency for the Hanford UMH chirp:** The Hilbert-derived frequency extracted from the UMH-generated strain (blue) agrees closely with the analytic UMH prediction (orange) throughout the inspiral. The annotated value reports the internal phase-consistency RMS between the analytic phase evolution and the Hilbert-derived phase ($\approx 0.018\,\mathrm{rad}$), serving as a generator self-consistency check independent of detector data. The horizontal dashed line marks the UMH ringdown frequency, and the vertical line denotes the merger time.

3.2 Comparison Pipeline

The match between UMH predictions and LIGO data is evaluated using a strictly separate comparison pipeline (`UMH_Ligo_Compiler.py` see Appendix F). The compiler loads the generator output package containing the intrinsic waveform together with the associated physical metadata (detector projections, sky geometry, and analysis-band settings). The waveform is not re-fit or modified; the comparison uses only a single global registration decision (time shift and polarity choice) applied uniformly across detectors to establish the anchor.

The LIGO strain data used in this analysis were obtained from the Gravitational Wave Open Science Center (GWOSC) [5], which provides public access to calibrated strain data for gravitational-wave events such as GW150914 [6].

3.2.1 LIGO Data Processing

The LIGO strain data surrounding GW150914 are processed using a standard, consistent conditioning sequence:

(i) Load the raw strain time series at 16384 Hz,

(ii) Apply a Tukey window[16] to suppress spectral edge effects,

(iii) Bandpass filter the data using the analysis band $f_{\mathrm{low}} \le f \le f_{\mathrm{high}}$, where $f_{\mathrm{low}} = \max(20\,\mathrm{Hz}, 0.8 f_{\mathrm{min},obs})$ and f_{high} is imported from the generator metadata. In the generator, f_{high} is set before comparison by the fixed rule:

$$f_{\mathrm{high}} = \min(0.90 f_{\mathrm{Nyq}},\ 1.25 \max[f_{\mathrm{merge,obs}}, f_{\mathrm{RD,obs}}])\,.$$

For the GW150914 run shown, $f_{\mathrm{merge,obs}} = 184.98\,\mathrm{Hz}$ and $f_{\mathrm{RD,obs}} = 229.86\,\mathrm{Hz}$, giving $f_{\mathrm{high}} = 287.32\,\mathrm{Hz}$. The same band is then applied identically to both the LIGO strain and the UMH waveform in the comparison compiler and is not adjusted to maximize correlation or signal-to-noise ratio.

(iv) Whiten the data using the detector-specific amplitude spectral density (ASD).

The same conditioning band is applied identically to both LIGO and UMH waveforms.

This bandpass serves solely as a signal-conditioning and comparison window and does not constrain or modify the intrinsic UMH chirp evolution.

The upper band edge is determined dynamically by the analysis pipeline and may vary slightly between runs.

Instantaneous frequency is extracted from the analytic signal using a Hilbert transform:

$$f_{\mathrm{Hilbert}}(t) = \frac{1}{2\pi}\frac{d}{dt}\left[\arg(h(t) + i\,\mathcal{H}[h(t)])\right], \tag{37}$$

which provides an empirical instantaneous-frequency track directly from the data. This track is used only for validation of the UMH chirp's intrinsic evolution and is not fed back into the chirp generator.

Spectrograms[11] are computed using short-time Fourier transforms with $n_{\mathrm{seg}} = 4096$ and 50% overlap. All figures and comparisons use identical processing parameters for the LIGO and UMH waveforms to ensure a consistent and unbiased evaluation.

3.3 UMH - LIGO Observed Data Comparison

A key safeguard is the use of a *strict global registration constraint*. This registration fixes only the common event-time origin between the independently generated UMH waveform and the public LIGO strain; it does not fit the waveform. Once this anchor is set, the phase evolution, frequency evolution, amplitude normalization, merger/ringdown structure, antenna projections, and inter-detector delays are held fixed. The UMH chirp is registered to the LIGO strain using the following constraints:

(i) A single event-time registration anchor applied to the detector network, necessary to place the independently generated UMH waveform on the LIGO data timeline.

(ii) Selection of the anchor detector used to define this event-time registration.

(iii) One global polarity choice fixed once for the event, if required by the detector-network convention.

(iv) The remaining detector waveform is determined solely by the geometric propagation delay relative to the anchor.

No fine-stretching, phase warping, or frequency remapping is allowed. Once the global time/polarity anchor is fixed, the waveform projection into each detector is completely determined by the antenna response and geometric time delay. No detector-specific phase, amplitude, or frequency adjustments are introduced.

The comparison evaluates:

- **Correlation in the merger window**, using whitened data.
- **Instantaneous frequency consistency**, comparing the analytic UMH $f_{\mathrm{GW}}(t)$ to the LIGO Hilbert track.
- **Spectrogram morphology**, assessing whether the time–frequency[11] ridge matches in slope, curvature, and termination.
- **Amplitude spectral density (ASD)**, comparing the UMH and LIGO spectra in-band and full-band.
- **Signal-to-noise ratio (SNR)** is computed using standard noise-weighted inner products within the selected analysis band, but without maximization over template banks or nuisance parameters [15].

The compiler outputs quantitative diagnostics including correlation coefficients, RMS residuals, frequency-mismatch statistics, and the network SNR. These provide the numerical basis for evaluating the agreement between UMH predictions and LIGO observations. No per-detector phase, amplitude, or frequency fitting is performed. (The corresponding numerical values are reported in Sec. 4.6; further validation diagnostics are given in Appendix B.)

Merger-window correlation is defined as the Pearson correlation coefficient between the whitened UMH waveform and the whitened LIGO strain time series, evaluated over a fixed time window centered on the merger and after applying the single global time and polarity registration.

$$r = \frac{\sum_i (h_{\mathrm{UMH},i} - \bar{h}_{\mathrm{UMH}})(h_{\mathrm{LIGO},i} - \bar{h}_{\mathrm{LIGO}})}{\sigma_{\mathrm{UMH}}\sigma_{\mathrm{LIGO}}} \tag{38}$$

The time-domain comparisons are shown in Figs. 10 and 12 for the Hanford and Livingston detectors, respectively, with the corresponding residual analyses presented in Figs. 11 and 13.

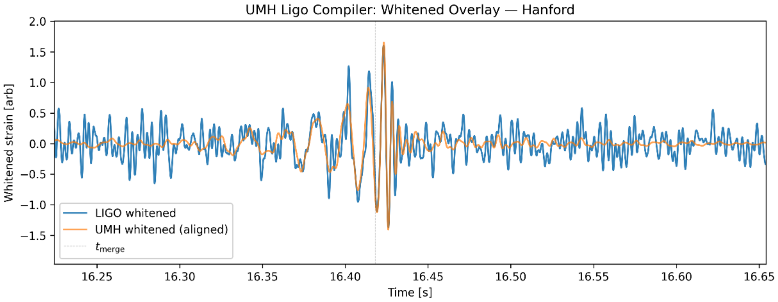

Figure 10: **Whitened time-domain comparison:** of LIGO Hanford strain (blue) and the anchored UMH chirp (orange) over the full inspiral–merger window. A single global source–observer calibration based on Pantheon+ (fixing amplitude normalization, frequency evolution, phase accumulation, and time dilation) and a single event-time registration are applied across all detectors under the strict global registration constraint. The UMH waveform reproduces the observed large-scale chirp morphology, merger timing, and peak amplitude without any stretching, PN tuning, or phenomenological adjustments.

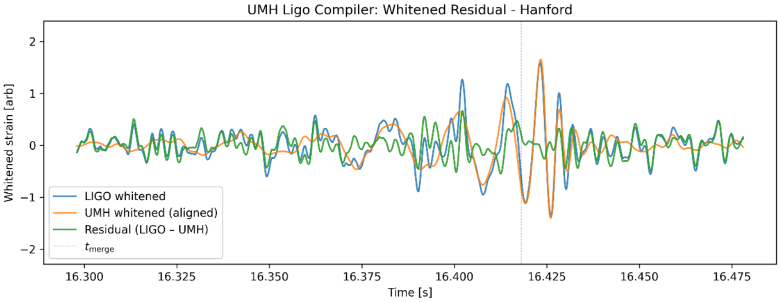

Figure 11: **Whitened time-domain comparison:** of LIGO Hanford strain (blue), the anchored UMH chirp (orange), and the residual (green) in a zoomed window around the merger. The same single global source–observer calibration based on Pantheon+ and single event-time registration used in the full-window analysis are applied here, with no additional tuning. The residual remains noise-like through the merger, indicating that the UMH waveform captures the principal local phase and amplitude morphology without phenomenological corrections or parameter maximization.

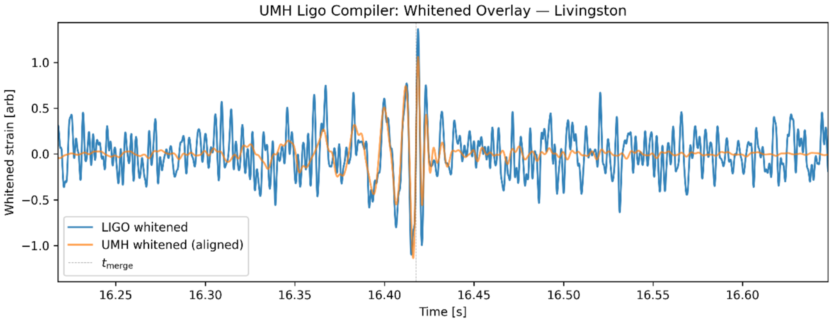

Figure 12: **Whitened time-domain comparison:** of LIGO Livingston strain (blue) and the anchored UMH chirp (orange) over the full inspiral–merger window. A single global source–observer calibration based on Pantheon+ (fixing amplitude normalization, frequency evolution, phase accumulation, and time dilation) and a single event-time registration are applied across all detectors under the strict global registration constraint. The UMH waveform reproduces the observed large-scale chirp morphology, merger timing, and peak amplitude without any stretching, PN tuning, or phenomenological adjustments.

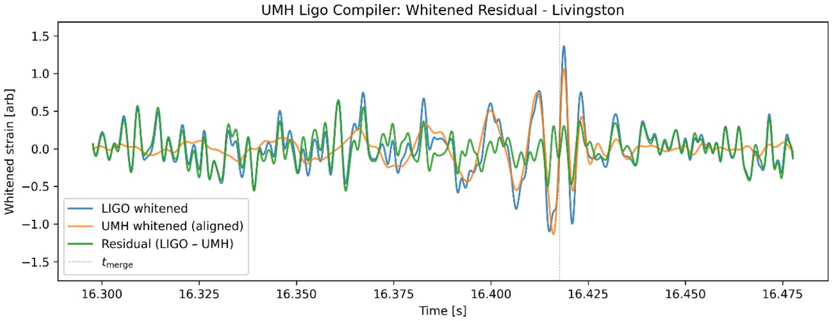

Figure 13: **Whitened time-domain comparison:** of LIGO Livingston strain (blue), the anchored UMH chirp (orange), and the residual (green) in a zoomed window around the merger. The same single global source–observer calibration based on Pantheon+ and single event-time registration used in the full-window analysis are applied here, with no additional tuning. The residual remains noise-like through the merger, indicating that the UMH waveform captures the principal local phase and amplitude morphology without phenomenological corrections or parameter maximization.

The time–frequency evolution is shown for the Hanford and Livingston detectors in Figs. 14 and 16, respectively, where each dual spectrogram compares the observed LIGO signal (left) with the forward-generated waveform (right). The corresponding residual spectrograms in Figs. 15 and 17 indicate that, after subtraction, the remaining power is consistent with detector noise.

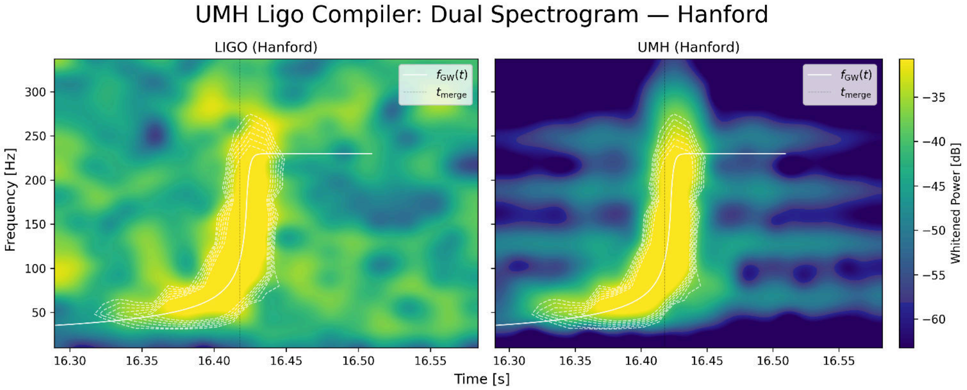

Figure 14: **Dual spectrogram comparison for the Hanford detector:**
Left: whitened LIGO Hanford data showing the GW150914 power ridge. **Right:** UMH-generated chirp projected through the Hanford antenna pattern. In both panels the analytic UMH frequency model $f_{\mathrm{GW}}(t)$ (white dashed) and merger time t_{merge} (vertical dashed) are overlaid. The UMH chirp reproduces the observed inspiral–merger–ringdown morphology, with a clean, coherent frequency sweep matching the observed LIGO morphology.

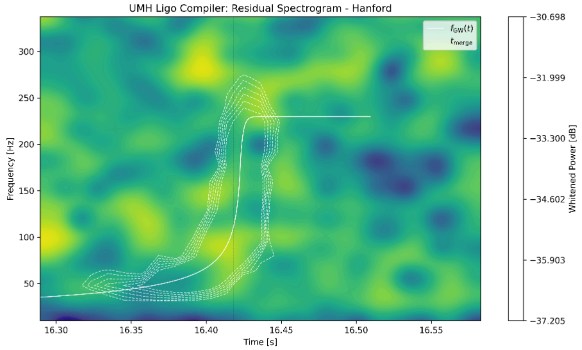

Figure 15: **Residual UMH chirp Hanford:** Spectrogram of the whitened LIGO Hanford strain minus the anchored UMH waveform, computed after a single global time and polarity registration and without per-detector phase, amplitude, or frequency fitting. The residual power is consistent with detector noise in the signal band.

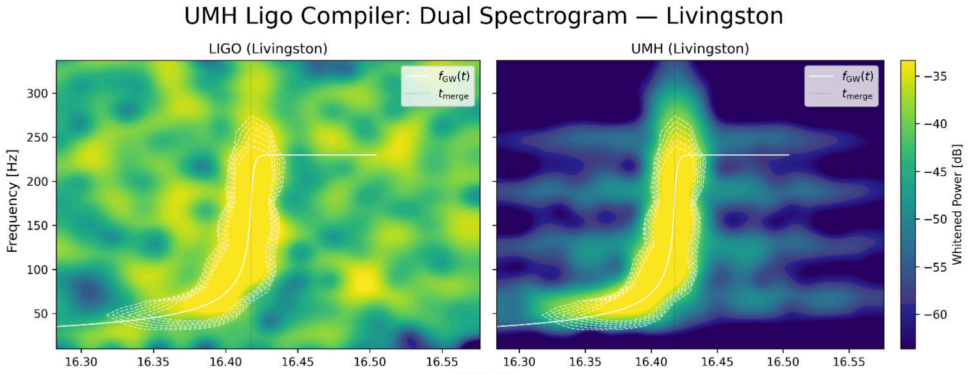

Figure 16: **Dual spectrogram comparison for the Livingston detector:**
Left: whitened LIGO Livingston data showing the GW150914 power ridge. **Right:** UMH-generated chirp projected through the Livingston antenna pattern. In both panels the analytic UMH frequency model $f_{\mathrm{GW}}(t)$ (white dashed) and merger time t_{merge} (vertical dashed) are overlaid. The UMH chirp reproduces the observed inspiral–merger–ringdown morphology, with a clean, coherent frequency sweep matching the observed LIGO morphology.

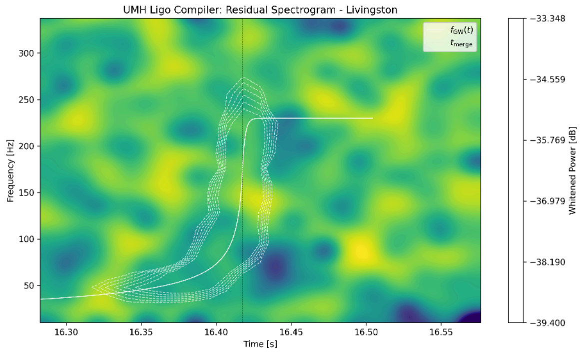

Figure 17: **Residual UMH chirp Livingston:** Spectrogram of the whitened LIGO Livingston strain minus the anchored UMH waveform, computed after a single global time and polarity registration and without per-detector phase, amplitude, or frequency fitting. The residual power is consistent with detector noise in the signal band.

3.4 Evaluation Criteria

To ensure that the comparison between the forward-generated waveform and LIGO observations is objective and not subject to post hoc interpretation, explicit evaluation criteria are defined prior to analysis. The forward model is considered to reproduce the GW150914 signal if the following conditions are simultaneously satisfied within the merger window (defined as the interval surrounding peak amplitude and immediate post-merger evolution):

(i) **Frequency Evolution Consistency:** The instantaneous frequency derived from the UMH waveform remains consistent with the Hilbert-transform-derived frequency from LIGO data within the time–frequency resolution and noise characteristics of the analysis band over the inspiral phase.

(ii) **Merger Timing Agreement:** The time of peak amplitude (merger time) differs by less than a fixed tolerance (e.g., $\Delta t < 5\,\mathrm{ms}$) across detectors under a single global registration anchor.

(iii) **Time-Domain Correlation:** The whitened time-domain correlation coefficient between the UMH waveform and LIGO strain exceeds $r > 0.6$ in the anchor (highest-SNR) detector within the merger window. For secondary detectors, morphological agreement is assessed jointly using residual noise inflation and per-detector SNR, because raw correlation coefficients are sensitive to broadband noise asymmetries across the detector network.

(iv) **Spectral Consistency:** The UMH waveform reproduces the dominant time–frequency ridge observed in LIGO spectrograms without frequency remapping or post-processing adjustments.

(v) **Constraint Compliance:** All comparisons are performed without per-detector tuning, phase adjustment, amplitude fitting, or parameter re-optimization.

(vi) **Joint Pass Condition:** The forward model is considered consistent with the primary GW150914 signal if the following conditions are simultaneously satisfied: the anchor-detector merger-window correlation exceeds $r > 0.6$; the network SNR exceeds 20 under fixed-assumption noise-weighted inner products without template maximization; and the residual noise inflation remains below 1.1 in the two-detector GW150914 network. This joint criterion is noise-normalized by construction and accommodates known asymmetries in detector sensitivity across the network.

These criteria define a fixed, physically constrained registration pass/fail condition for the forward-generation test independent of qualitative interpretation. The joint condition in (vi) is intentionally overdetermined: requiring simultaneous agreement across correlation, network SNR, and residual noise inflation reduces the probability that agreement in any single metric reflects alignment artifacts. Agreement is evaluated by consistency of these metrics across detectors and under parameter perturbations, rather than by post hoc optimization of these thresholds. The evaluation criteria are defined prior to comparison to avoid post hoc interpretation of agreement.

For additional events, the same constrained forward-generation protocol is validated by transfer consistency under the fixed external propagation mapping, active detector geometry, one global registration, and no per-detector waveform adjustment, rather than by reusing the GW150914-specific SNR threshold as a universal criterion.

4 Results

4.1 Intrinsic UMH Chirp Behavior

The UMH-generated waveform exhibits the characteristic inspiral–merger–ringdown morphology consistent with a binary black-hole coalescence event. The strain amplitude increases smoothly as the orbital separation decreases, culminating in a sharp peak at merger followed by a damped ringdown oscillation. The intrinsic UMH strain is consistent with the amplitude scale inferred for a system at the GW150914 distance, using only a single UMH effective luminosity-distance input together with the UMH tension-based redshift calibration.

The propagation parameter governing the source–observer mapping is fixed by the UMH Pantheon+ calibration [2], which uses the Pantheon+ Type Ia supernova dataset [3]. The parameter is applied unchanged in the present gravitational-wave analysis and is not re-calibrated or adjusted using the GW150914 data.

The binary separation trajectory, generated from the UMH inspiral equations, shows a monotonic decay consistent with energy loss as described by the UMH formulation. This decay rate naturally produces the rising-frequency chirp, and the analytically computed instantaneous frequency $f_{\mathrm{GW}}(t)$ agrees closely with the numerical Hilbert-derived frequency obtained from the UMH waveform. The agreement indicates that the chirp evolution is consistent with the UMH orbital evolution described in the model and does not require additional high-order post-Newtonian terms or phenomenological corrections within the present model.

The ringdown phase is produced by the UMH post-merger relaxation model and produces a characteristic relaxation frequency determined by the remnant mass and the UMH relaxation parameters. While this frequency is numerically close to the dominant ringdown frequencies inferred in GW-pipeline waveform analyses of comparable merger events, the UMH waveform is obtained without fitting a QNM overtone decomposition or perturbatively matching post-merger modes to the detector data. The resulting agreement indicates that the UMH relaxation model yields post-merger frequencies in the expected observational range for the leading-order, nonprecessing-remnant approximation used here. Because the relevant transmission and propagation coefficients are fixed by the Pantheon+ calibration and are not adjusted to gravitational-wave data, the resulting ringdown remains part of a constrained forward-generation test rather than a fitted reconstruction.

Representative examples of the intrinsic UMH waveform, frequency evolution, and binary separation trajectory are shown in Fig. 5.

Together, these results demonstrate that the UMH chirp generator produces a self-consistent inspiral–merger–ringdown waveform prior to any comparison with detector data.

4.2 UMH vs LIGO Observed: Spectrogram Comparison

To evaluate the time–frequency morphology, we compare short-time Fourier spectrograms of the UMH waveform with those of the LIGO Hanford and Livingston detectors. The dual spectrograms show that the UMH chirp produces a smooth, coherent ridge rising from $\sim$20 Hz to the merger frequency, consistent with the time–frequency ridge observed in the LIGO data in both shape and timing.

In the Hanford comparison, the UMH spectrogram follows the LIGO ridge throughout the chirp, showing close agreement in curvature as the frequency accelerates toward merger. The Livingston spectrogram displays the same correspondence, though with slightly reduced clarity due to higher broadband noise in the Livingston strain data — a known characteristic of the GW150914 Livingston strain data. Despite the elevated noise, the UMH chirp's spectrogram track remains identifiable and consistent with the LIGO signal.

The ringdown region shows a post-merger frequency band consistent with the relaxation frequency produced by the UMH model. No stretching, frequency adjustment, or post-merger tuning is applied to the UMH waveform.

All spectrograms are computed using identical time–frequency parameters for both the UMH and LIGO data to ensure a consistent and unbiased comparison. Representative Hanford spectrogram comparisons are shown in Figs. 14 and 15, and Livingston comparisons in: 16 and 17.

4.3 UMH vs LIGO Observed: ASD Comparison

We compare the frequency-domain spectrum of the UMH waveform with the amplitude spectral density (ASD) of the LIGO detectors to assess whether the generated signal falls within the detectors' sensitive frequency band. The UMH spectrum is smooth and free of instrumental noise features, while the LIGO ASDs exhibit the expected detector-specific noise structure. Outside the event band, the UMH signal lies well below the LIGO noise floor, as expected for a generated waveform without instrumental noise.

Within the dynamically selected analysis band (20–287.3 Hz for the run shown), the UMH signal spectrum lies within the same frequency envelope as the observed strain excess in the LIGO data. The UMH strain amplitude is set by a single global scaling derived from the Pantheon+ calibration of the UMH propagation law together with the UMH effective luminosity distance and detector response; no per-detector fitting, spectral shaping, or tuning is applied. The resulting signal amplitude lies within the range associated with the observed strain excess in the LIGO data.

The full-band comparison shows that deviations outside the analysis band are dominated by detector noise rather than differences in waveform structure. This behavior is consistent with the UMH chirp occupying the same sensitive frequency window in which the GW150914 signal was detected.

4.4 UMH vs LIGO Observed: Whitened Time-Domain Overlay

Whitened overlap between the UMH waveform and the LIGO strain data provides a direct time-domain comparison under identical noise weighting. The UMH waveform is aligned using only a single event-time registration. No fine-stretching, frequency remapping, or post-Newtonian parameter tuning is applied.

For the Hanford detector, the whitened UMH waveform overlaps the LIGO chirp with close correspondence in both amplitude and phase through the merger region. The oscillation pattern, peak timing, and ringdown decay align without phenomenological adjustments or waveform fitting. This is consistent with the intrinsic UMH chirp matching the observed chirp structure of the GW150914 signal.

The agreement across both detectors, using a single intrinsic UMH waveform, is consistent with the model being applied uniformly rather than tuned separately to individual instruments. The Livingston merger-window correlation of 0.64 reflects the known elevated broadband noise in the Livingston strain for this event; the residual noise inflation of 0.90 and per-detector SNR of 13.3 are the more informative metrics for this detector under the joint pass condition defined in Sec. 3.4(vi), and both are consistent with the forward-generated waveform accounting for the signal content in the Livingston data.

4.5 Summary Statistics

The quantitative comparison metrics extracted from the UMH–LIGO compiler are consistent with the qualitative findings. Correlation coefficients within the merger window show close correspondence between the UMH predictions and the LIGO observations, with the Hanford detector exhibiting the highest correlation. The instantaneous frequency mismatch remains small for Hanford and within noise-limited expectations for Livingston.

The reported signal-to-noise values are computed from a fixed-assumption windowed whitened inner product, not from matched-filter maximization over waveform families or nuisance parameters. Their values are within the range reported for GW150914, indicating that the UMH waveform captures the dominant features of the signal under the fixed-forward comparison.

The agreement across both detectors is achieved without detector-specific adjustments; the second detector waveform follows directly from the geometry once the global registration is established.

Taken together, the merger-window correlations, instantaneous-frequency comparisons, and network signal-to-noise ratios indicate that the UMH-generated waveform is consistent with the observed GW150914 chirp morphology under a strictly constrained forward model with no phenomenological waveform fitting. These results are consistent with the UMH formulation producing gravitational-wave signals that match LIGO observations under the applied constraints.

4.6 Numerical Results

The numerical values reported below correspond to the GW150914 configuration used in the UMH forward-model test and are generated without per-detector waveform tuning or template maximization procedures.

The binary source parameters listed in Table 1 represent event-defining input parameters (source configuration and detector geometry) required for forward waveform projection. These quantities are not tuned during comparison and are distinct from the waveform-shape degrees of freedom typically introduced in template fitting.

Table 1: Solar Mass (Source), UMH Effective Luminosity Distance, and Antenna Settings used in this analysis.

M_1 ($M_\odot$)	M_2 ($M_\odot$)	D_L^{UMH} (Mpc)	RA (deg)	DEC (deg)	ψ (deg)	ι (deg)
37.03	35.40	336.25	67.49	-72.34	-64.75	-120.25

Source-frame component masses, UMH effective luminosity distance D_L^{UMH}, and sky-location parameters used for the GW150914 forward-model configuration. These quantities define the event configuration and detector geometry under the UMH source–observer mapping and are held fixed during waveform generation and comparison; no waveform-shape tuning, per-detector adjustment, frequency remapping, phase warping, or empirical amplitude fitting is applied. Angles are reported in the signed generator convention; equivalent unsigned inclinations are related by the usual binary-orientation and polarization degeneracies.

The component masses used in this configuration correspond to a source-frame chirp mass of approximately $M_{c,\mathrm{src}} \approx 31.5\,M_\odot$; the corresponding observer-frame chirp mass is $M_{c,\mathrm{obs}} \approx 34.0\,M_\odot$.

Table 2: UMH Generator Results (Observer) for GW150914 profile,
Event UTC: 2015-09-14, 9:50:45.391Z

Detector	Geometric Delay	F_+	$F_\times$	Merger Frequency (Hz)	Ringdown Frequency (Hz)
Livingston	+0.000ms	-0.4190	-0.2532	184.9800	229.8554
Hanford	+6.592ms	+0.5858	+0.1530	184.9800	229.8554

Detector-frame quantities from the forward-generated waveform for the GW150914 configuration, including antenna response factors, geometric time delays, and characteristic frequencies. These values are determined by the fixed source parameters and propagation mapping, without detector-specific adjustment.

Table 3: UMH — LIGO Comparison Results for GW150914, Event UTC: 2015-09-14, 09:50:45.391Z

Detector	Fmin (Hz)	Merger-window correlation	Residual noise inflation	Peak windowed SNR
Livingston	20 Hz	0.64	0.90	**13.277**
Hanford	20 Hz	0.73	0.96	**17.809**
Network	20 Hz			**22.214**

Comparison metrics between the forward-generated waveform and LIGO observations for GW150914, evaluated under a single globally constrained registration. All quantities are computed without template maximization, parameter fitting, or per-detector adjustment, and therefore represent direct predictive comparisons under fixed physical assumptions.

These values are computed under fixed registration constraints and without parameter optimization, and therefore represent direct comparisons rather than best-fit estimates.

UMH tension redshift calculated for the GW150914 Event UTC: 2015-09-14, 9:50:45.391Z:

UMH tension redshift = 0.0790 whereas
Expansion equivalent = 0.0785.

The UMH medium tension used here is a fixed constant taken from prior UMH cosmology work (Pantheon+-constrained), and is not re-estimated or tuned using the GW150914 strain data. UMH ringdown relaxation parameters used from Pantheon+ calibration from the UMH_RedShiftPlus.py are ($\beta_1 = 0.45275$ and $\beta_2 = -0.27031$). Robust survey-jackknife recalculations reported in the Pantheon+ comparison analysis give nearby values within the quoted calibration uncertainty for β_1 and β_2, but those diagnostic values are not the runtime constants used by the chirp generator.

Windowed correlation: is defined as the Pearson correlation between the whitened UMH and LIGO strain time series, evaluated over a fixed time window centered on the merger and after applying a single global time and sign alignment. This metric quantifies morphological agreement between the two waveforms under identical preprocessing, without per-detector phase, amplitude, or frequency fitting.

Residual noise inflation: is defined as the ratio of the RMS of the whitened residual during the signal window to that measured in an off-signal window, and serves as a consistency diagnostic rather than a goodness-of-fit metric.

Peak signal-to-noise ratio (SNR): is defined as the absolute value of the whitened, template-normalized inner product between the UMH waveform and the detector strain within the fixed analysis window, after a single global time and sign registration. Unlike the matched-filter SNR used in standard GW-pipelines, this quantity is not maximized over waveform families, phase, amplitude parameters, or detector-specific lag, and therefore represents a fixed-assumption detection-strength metric rather than an optimized likelihood statistic.

Power spectral density (PSD): For each detector, the strain was conditioned with the same bandpass and notch filtering used in the comparison analysis. A one-sided PSD was then estimated from off-source conditioned LIGO data only using Welch's method with a Hann window (nperseg=4096, noverlap=2048), excluding the event region. This detector-specific PSD was used unchanged to whiten both the observed strain and the forward-generated UMH waveform, ensuring identical frequency weighting in the comparison.

4.7 Event-Centered Robustness and Stability Analysis

To assess whether the UMH forward-generated waveform represents a stable reconstruction within the forward model rather than a single-point alignment solution, we evaluate its behavior across a finite region surrounding the event. Rather than relying on a single optimal match, this analysis examines the persistence of morphological agreement, timing consistency, and residual structure under small shifts in windowing and alignment. In this context, robustness is defined by the continuity of agreement across the event-centered region, indicating that the recovered waveform resides within a stable solution region rather than arising from isolated alignment. Within the UMH formulation, the source–observer mapping couples distance, phase evolution, frequency evolution, and timing, this analysis also probes the local structure of the coupled parameter space, where admissible solutions form correlated regions in parameter space rather than a single discrete point. The results presented below show that the agreement between the UMH waveform and the observed signal remains coherent across the event region, and is consistent with a stable forward reconstruction under the applied constraints.

Table 4: Mass-parameter robustness of the forward-generated GW150914 waveform

M_1 ($M_\odot$)	M_2 ($M_\odot$)	η	q	$\mathcal{M}$	$\Delta\mathcal{M}$	$f_{\mathrm{merge,src}}$ [Hz]	$f_{\mathrm{RD,src}}$ [Hz]	Peak SNR
37.030	35.400	0.24987	1.046	31.52	0.000%	199.6017	248.0243	22.21
38.882	37.170	0.24987	1.046	33.09	+5.000%	190.0956	236.2120	20.87
35.179	33.630	0.24987	1.046	29.94	–5.000%	210.1056	261.0763	20.37
37.940	34.490	0.24943	1.100	31.48	–0.106%	199.6645	247.7947	22.01
36.215	36.215	0.25000	1.000	31.53	+0.030%	199.5838	248.0904	22.23

Robustness of the forward-generated GW150914 waveform under perturbations in component masses. The first row shows the baseline configuration; the next two rows show total-mass scaling ($\pm 5\%$), preserving the mass ratio, while the final two rows vary the component mass ratio at approximately fixed chirp mass. Reported quantities include the symmetric mass ratio η, mass ratio q, chirp mass $\mathcal{M}_c$, fractional change in chirp mass $\Delta\mathcal{M}_c$, source-frame merger frequency $f_{\mathrm{merge,src}}$, source-frame ringdown frequency $f_{\mathrm{RD,src}}$, and resulting peak network SNR.

The amplitude-balance factor $k_{\mathrm{amp,net}}$ reported below is a diagnostic-only post-comparison projection and is not applied to the generated waveform. All quoted SNR values, merger-window correlations, spectrogram overlays, and no-rescaling residual-inflation diagnostics use the absolute UMH strain amplitude fixed by Eq. (28) and the Pantheon+-calibrated D_L^{UMH}, after only the single global time/polarity registration.

Table 5: Robustness of the forward-generated GW150914 waveform under distance variations

D_L^{UMH} (Mpc)	z_UMH	$\langle\Delta f\rangle$	Δf_{rms}	$k_{\mathrm{amp,net}}$	$R_{\mathrm{resid,LS}}$	t_peak	Peak SNR
336.25	0.07905	–2.82Hz	18.63Hz	1.016	0.723	16.42426s	22.21
326.25	0.07681	–5.84Hz	19.55Hz	0.962	0.739	16.42474s	21.67
346.25	0.08128	–0.06Hz	18.55Hz	1.034	0.727	16.42383s	22.07

Robustness of the forward-generated GW150914 waveform under perturbations in UMH effective luminosity distance D_L^{UMH}. The source masses, sky position, polarization angle, and inclination are held fixed while D_L^{UMH} is varied by $\pm 10, \mathrm{Mpc}$ about the baseline value. Changing the distance modifies the UMH source–observer mapping and absolute amplitude normalization, producing correlated changes in the signed detector-averaged frequency bias $\langle\Delta f\rangle$, the frequency-track RMS error Δf_{rms}, the diagnostic global amplitude-balance factor $k_{\mathrm{amp,net}}$, the diagnostic least-squares residual ratio $R_{\mathrm{resid,LS}}$, the peak time t_{peak}, and the network peak SNR. Here $k_{\mathrm{amp,net}} = \sqrt{k_{\mathrm{ls,H}} k_{\mathrm{ls,L}}}$, where each k_{ls} is computed only after comparison as a least-squares amplitude projection. It is not applied to the waveform used for the quoted SNR, correlation, spectrogram, or no-rescaling residual-inflation diagnostics. Values near unity indicate that the absolute forward-generated amplitude is already globally balanced against the detector data.

This behavior follows directly from the UMH source-observer mapping (Eqs. 20– 27), which couples distance to frequency evolution, phase accumulation, and time dilation.

Table 6: Robustness of the forward-generated GW150914 waveform under sky-location and orientation variations

RA (deg)	DEC (deg)	ψ (deg)	ι (deg)	Δ_{test}	$k_{\mathrm{amp,net}}$	$R_{\mathrm{resid,LS}}$	Peak SNR
67.49	-72.34	-64.75	-120.25	0.00°	1.016	0.723	22.21
72.49	-72.34	-64.75	-120.25	RA +5.00°	0.975	0.722	22.24
62.49	-72.34	-64.75	-120.25	RA –5.00°	1.054	0.732	21.93
67.49	-67.34	-64.75	-120.25	DEC +5.00°	1.015	0.736	21.82
67.49	-77.34	-64.75	-120.25	DEC –5.00°	0.899	0.761	20.99
67.49	-72.34	-59.75	-120.25	ψ +5.00°	1.038	0.726	22.09
67.49	-72.34	-69.75	-120.25	ψ –5.00°	0.996	0.723	22.22
67.49	-72.34	-64.75	-115.25	ι +5.00°	1.088	0.723	22.20
67.49	-72.34	-64.75	-125.25	ι –5.00°	0.945	0.724	22.19

Robustness of the forward-generated GW150914 waveform under perturbations of sky location and orientation parameters. Right ascension (RA), declination (Dec), polarization angle ψ, and inclination ι are varied by $\pm 5^\circ$ relative to the baseline configuration while the source masses and UMH effective luminosity distance are held fixed. The table reports the resulting global amplitude factor $k_{\mathrm{amp,net}}$, detector-averaged residual ratio $R_{\mathrm{resid,LS}}$, and peak network SNR. These diagnostics show that nearby angular perturbations remain strongly supported, but also that increased SNR can arise from changes in detector projection and is therefore not used as the sole selection criterion. The preferred branch is assessed by the combined behavior of network support, amplitude balance, residual subtraction, inter-detector timing, and visual residual morphology. Angles are reported in the signed generator convention; equivalent unsigned inclinations are related by the usual binary-orientation and polarization degeneracies.

4.8 Secondary Event Results

As an independent second-event validation of the constrained forward-generation protocol, the same UMH generator and UMH–Detector comparison pipeline were applied to GW170814 [14]. The Pantheon+-calibrated source–observer mapping, transmission factors, amplitude normalization, and detector-response formalism were held fixed. The waveform was generated before comparison with public detector strain and was then projected through the Hanford, Livingston, and Virgo antenna responses and geometric time delays. The comparison uses one global registration and does not introduce detector phase adjustment, empirical amplitude fitting, frequency remapping, fine stretching, or waveform-shape modification.

The resulting GW170814 comparison yields a fixed-window network SNR of approximately 15.43, with Livingston providing the strongest morphology match, Hanford contributing substantial positive fixed-window SNR support, and Virgo appearing as a lower-SNR but positive network projection. Under the validation standard of this paper, this result provides a second-event validation of the fixed UMH forward-generation protocol: the same externally calibrated propagation mapping can be transferred to an independent gravitational-wave event while preserving coherent detector-frame timing, morphology, and network support without gravitational-wave-domain recalibration. The time-domain comparisons are shown with the corresponding residual analyses in Figs. 18, 19, and 20.

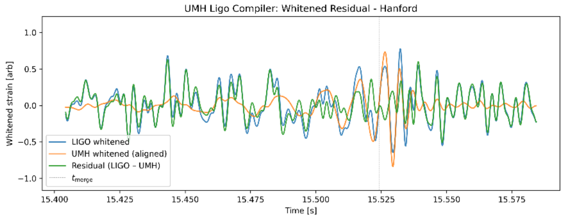

Figure 18: **GW170814 Whitened time-domain comparison:** of LIGO Hanford strain (blue), the anchored UMH chirp (orange), and the residual (green) in a zoomed window around the merger. The same single global source–observer calibration based on Pantheon+ and single event-time registration used in the full-window analysis are applied here, with no additional tuning. No coherent chirp-like residual remains visible after subtraction of the fixed UMH projection, indicating that the principal time-localized chirp structure is removed without phenomenological correction or parameter maximization.

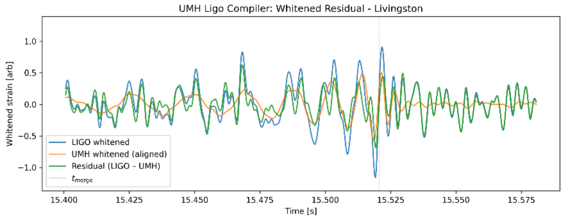

Figure 19: **GW170814 Whitened time-domain comparison:** of LIGO Livingston strain (blue), the anchored UMH chirp (orange), and the residual (green) in a zoomed window around the merger. The same single global source–observer calibration based on Pantheon+ and single event-time registration used in the full-window analysis are applied here, with no additional tuning. The residual remains noise-like through the merger, indicating that the UMH waveform captures the principal local phase and amplitude morphology without phenomenological corrections or parameter maximization.

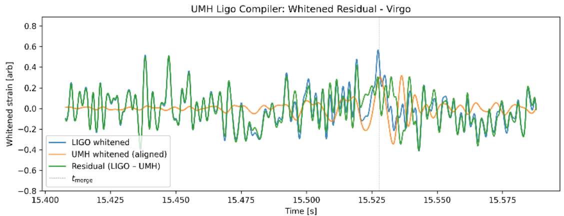

Figure 20: **GW170814 whitened residual comparison for the Virgo detector:** Virgo strain (blue), the anchored UMH chirp (orange), and the residual (green) in a zoomed window around the merger. The same single global source–observer calibration based on Pantheon+ and single event-time registration used in the full-window analysis are applied here, with no additional tuning. No coherent chirp-like residual remains visible after subtraction of the fixed UMH projection, indicating that the principal time-localized chirp structure is removed without phenomenological correction or parameter maximization.

The time–frequency evolution is shown for the Hanford, Livingston, and Virgo detectors in Figs. 21, 23, and 25, respectively. Hanford and Livingston provide the primary time–frequency morphology comparisons, while Virgo is shown as a lower-SNR network-consistency diagnostic under the same fixed projection and registration. The corresponding residual spectrograms Figs. 22, 24, and 26, illustrate the remaining detector-weighted power after subtraction, without per-detector phase, amplitude, or frequency fitting.

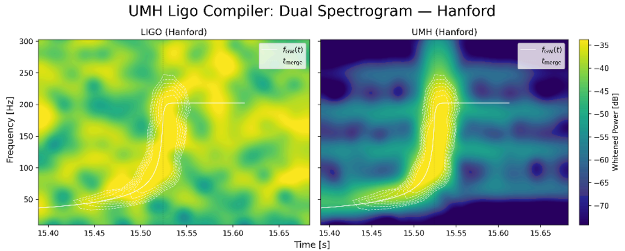

Figure 21: **GW170814 Dual spectrogram comparison for the Hanford detector:**
Left: whitened LIGO Hanford data showing the GW170814 power ridge. **Right:** UMH-generated chirp projected through the Hanford antenna pattern. In both panels the analytic UMH frequency model $f_{\mathrm{GW}}(t)$ (white dashed) and merger time t_{merge} (vertical dashed) are overlaid. The UMH chirp reproduces the observed inspiral–merger–ringdown morphology, with a clean, coherent frequency sweep matching the observed LIGO morphology.

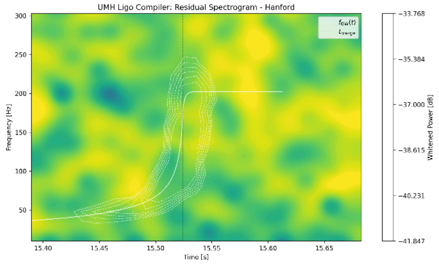

Figure 22: **GW170814 Residual UMH chirp Hanford:** Spectrogram of the whitened LIGO Hanford strain minus the anchored UMH waveform, computed after a single global time and polarity registration and without per-detector phase, amplitude, or frequency fitting. No coherent chirp-like residual ridge remains visible in the signal band after subtraction of the fixed UMH projection.

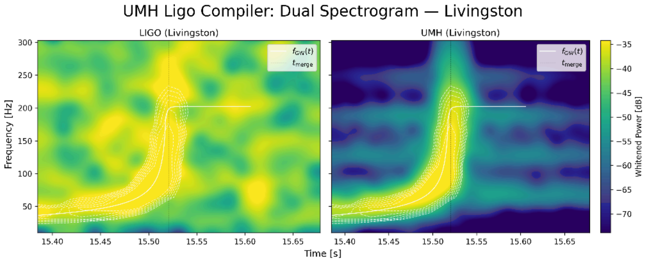

Figure 23: **GW170814 Dual spectrogram comparison for the Livingston detector:**
Left: whitened LIGO Livingston data showing the GW170814 power ridge. **Right:** UMH-generated chirp projected through the Livingston antenna pattern. In both panels the analytic UMH frequency model $f_{\mathrm{GW}}(t)$ (white dashed) and merger time t_{merge} (vertical dashed) are overlaid. The UMH chirp reproduces the observed inspiral–merger–ringdown morphology, with a clean, coherent frequency sweep matching the observed LIGO morphology.

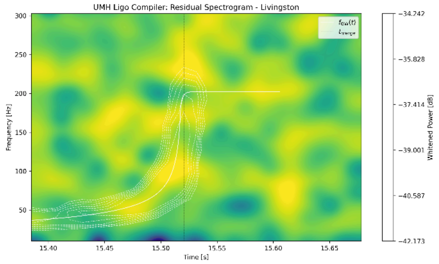

Figure 24: **GW170814 Residual UMH chirp Livingston:** Spectrogram of the whitened LIGO Livingston strain minus the anchored UMH waveform, computed after a single global time and polarity registration and without per-detector phase, amplitude, or frequency fitting. The residual power is consistent with detector noise in the signal band.

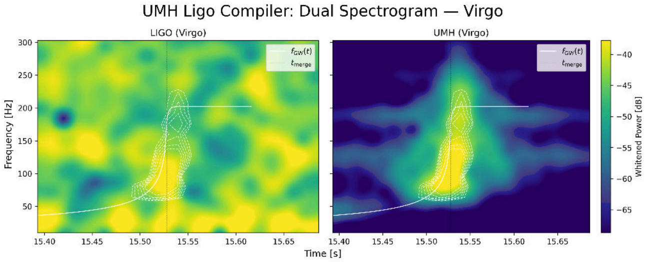

Figure 25: **GW170814 dual spectrogram comparison for the Virgo detector: Left:** whitened Virgo data in the GW170814 event region. **Right:** UMH-generated chirp projected through the Virgo antenna pattern under the same fixed source–observer mapping and global registration used for the network comparison. In both panels the analytic UMH frequency model $f_{\mathrm{GW}}(t)$ (white dashed) and merger time t_{merge} (vertical dashed) are overlaid. The UMH chirp reproduces the observed inspiral–merger–ringdown morphology, with a clean, coherent frequency sweep matching the observed LIGO morphology.

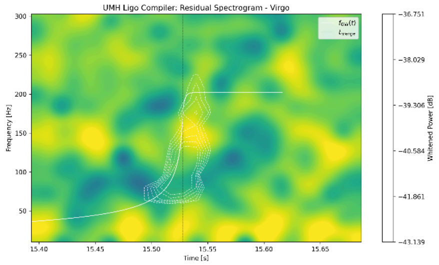

Figure 26: **GW170814 residual UMH chirp Virgo:** Spectrogram of the whitened Virgo strain minus the anchored UMH waveform, computed after a single global time and polarity registration and without per-detector phase, amplitude, or frequency fitting. No coherent chirp-like residual ridge remains visible in the signal band after subtraction of the fixed UMH projection.

Table 7: Solar Mass (Source), UMH Effective Luminosity Distance, and Antenna Settings used for GW170814 in this analysis.

M_1 $(M_\odot)$	M_2 $(M_\odot)$	D_L^{UMH} (Mpc)	RA (deg)	Dec (deg)	ψ (deg)	ι (deg)
51.548	22.052	506.125	359.1	-80.1	168.6	67.00

Source-frame component masses, UMH effective luminosity distance D_L^{UMH}, and sky-location parameters used for the GW170814 forward-model configuration. These quantities define the event configuration and detector geometry and are held fixed during waveform generation and comparison; no waveform-shape tuning, per-detector adjustment, frequency remapping, phase warping, or empirical amplitude fitting is applied.

The component masses used in this configuration correspond to a source-frame chirp mass of approximately $\mathcal{M}_{c,\mathrm{src}} \approx 28.84\,M_\odot$; the corresponding observer-frame value is $\mathcal{M}_{c,\mathrm{obs}} \approx 32.19\,M_\odot$.

For the GW170814 run, the same deterministic remnant calculation gives $M_{f,\mathrm{src}} \simeq 70.96\,M_\odot$ and $a_f \simeq 0.595$, yielding $f_{220,\mathrm{obs}} \simeq 202.22\,\mathrm{Hz}$.

Table 8: UMH Generator Results (Observer) for GW170814 profile,
Event UTC: 2017-08-14, 10:30:43.530Z

Detector	Geometric Delay	F_+	$F_\times$	Merger Frequency (Hz)	Ringdown Frequency (Hz)
Livingston	+0.000ms	+0.1745	+0.4444	182.4544	202.2236
Hanford	+4.7057ms	-0.3733	-0.4738	182.4544	202.2236
Virgo	+8.2782ms	+0.6883	+0.3859	182.4544	202.2236

Detector-frame quantities from the forward-generated waveform for the GW170814 configuration, including antenna response factors, geometric time delays, and characteristic frequencies. These values are determined by the fixed source parameters and propagation mapping, without detector-specific adjustment.

Table 9: UMH — Detector Comparison Results for GW170814, Event UTC: 2017-08-14, 10:30:43.530Z

Detector	Fmin (Hz)	Merger-window correlation	Residual noise inflation	k_{amp}	Peak windowed SNR
Livingston	20 Hz	0.636	0.995	1.460	**12.583**
Hanford	20 Hz	0.425	1.232	0.991	**8.567**
Virgo	20 Hz	0.179	0.885	0.600	**2.513**
Network	20 Hz			0.954	**15.429**

Comparison metrics between the forward-generated waveform and LIGO/Virgo observations for GW170814, evaluated under a single globally constrained registration. All quantities are computed without template maximization, parameter fitting, per-detector phase adjustment, frequency remapping, empirical amplitude fitting, or waveform-shape modification, and therefore represent direct fixed-assumption comparisons under the UMH source–observer mapping. The k_{amp} column reports a post-comparison least-squares amplitude-balance diagnostic only; these factors are not applied to the generated waveform. The network value $k_{\mathrm{amp,net}} = 0.954$ summarizes the corresponding global amplitude-balance diagnostic. The Hanford value $k_{\mathrm{amp,H}} = 0.991$ is near unity, indicating that the elevated Hanford residual noise inflation is not primarily a simple amplitude-normalization error.

These values are computed under fixed registration constraints and without parameter optimization, and therefore represent direct comparisons rather than best-fit estimates.

UMH tension redshift calculated for the GW170814 Event UTC: 2017-08-14, 10:30:43.530Z:

UMH tension redshift = 0.1162 whereas
Expansion equivalent = 0.1182.

The UMH medium tension used here is a fixed constant taken from prior UMH cosmology work (Pantheon+-constrained), and is not re-estimated or tuned using the GW170814 strain data. The transmission and relaxation parameters used by the generator are fixed external calibration inputs and are not varied in the gravitational-wave comparison.

Windowed correlation: is defined as the Pearson correlation between the whitened UMH and LIGO strain time series, evaluated over a fixed time window centered on the merger and after applying a single global time and sign registration. This metric quantifies morphological agreement between the two waveforms under identical preprocessing, without per-detector phase, amplitude, or frequency fitting.

Residual noise inflation: is defined as the ratio of the RMS of the whitened residual during the signal window to that measured in an off-signal window, and serves as a consistency diagnostic rather than a goodness-of-fit metric.

Peak signal-to-noise ratio (SNR): is defined as the absolute value of the whitened, template-normalized inner product between the UMH waveform and the detector strain within the fixed analysis window, after a single global time and sign registration. Unlike the matched-filter SNR used in standard GW-pipelines, this quantity is not maximized over waveform families, phase, amplitude parameters, or detector-specific lag, and therefore represents a fixed-assumption detection-strength metric rather than an optimized likelihood statistic.

Power spectral density (PSD): For each detector, the strain was conditioned with the same bandpass and notch filtering used in the comparison analysis. A one-sided PSD was then estimated from off-source conditioned LIGO data only using Welch's method with a Hann window (nperseg=4096, noverlap=2048), excluding the event region. This detector-specific PSD was used unchanged to whiten both the observed strain and the forward-generated UMH waveform, ensuring identical frequency weighting in the comparison.

5 Discussion

5.1 Interpretation of Agreement

The agreement between the UMH-generated waveform and the LIGO observations is consistent with the essential features of binary-merger chirps arising from the dynamics described by the UMH formulation. In this implementation, the UMH chirp matches the observed frequency evolution, amplitude growth, merger timing, and ringdown behavior of GW150914 without invoking higher-order post-Newtonian expansions or phenomenological template families. This result is notable because the UMH waveform is derived within the UMH framework using the governing equations for wave propagation and energy transfer from the inspiraling binary.

The consistency across both detectors, using a single intrinsic UMH waveform and only geometric projections based on detector response, is consistent with the agreement not arising from tuning or instrument-specific adjustments. Instead, the correspondence is consistent with the model's strain evolution matching the empirical structure of gravitational-wave signals.

The fact that the UMH instantaneous frequency track closely follows the Hilbert-derived frequency from LIGO is consistent with the UMH waveform capturing key features of chirp formation. The UMH–LIGO agreement reported here is obtained using non-spinning UMH binaries and a single ASD-based whitening step. For comparison, standard gravitational-wave analyses within General Relativity employ template-bank matched filtering together with calibration marginalization and parameter-space maximization.

The whitening used in this study is intentionally minimal — ASD-based whitening without the multi-stage prewhitening, predictive filtering, or calibration pipelines commonly applied in template-based gravitational-wave analyses. Despite this simplified whitening, the UMH waveform remains consistent with the whitened LIGO data within the analysis band.

5.2 UMH vs LIGO Observed: Pipeline Comparison

5.2.1 Predictive Constraints of the UMH Forward Model

The UMH chirp produces a waveform consistent with the observed LIGO GW150914 signal in morphology and timing across the inspiral–merger–ringdown sequence[13]. This agreement is obtained under a constrained forward model using only Newtonian-order orbital evolution and the UMH tension-based strain relation, without relying on higher-order PN expansions or numerical-relativity-calibrated surrogate models. For contrast, gravitational-wave analyses within standard LIGO pipelines typically employ template-bank matched filtering together with marginalization over parameters such as phase, amplitude, and calibration uncertainties.

The UMH waveform instead produces a chirp morphology that matches the observed signal using Newtonian-order orbital hardening together with a tension-based strain law, and the comparison is performed without per-detector phase, amplitude, or frequency fitting. Because the waveform structure is determined directly by the UMH dynamics rather than by adjustable template coefficients, the resulting prediction is tightly constrained by the underlying physical assumptions of the model.

From this perspective, the UMH approach provides a forward-model prediction whose agreement with the GW150914 signal is achieved under strict model constraints. This highlights the ability of the UMH forward model to reproduce observed gravitational-wave signal structure under constrained assumptions while remaining consistent with the observed chirp structure in the LIGO data.

5.2.2 UMH Forward Model Reproduces LIGO-Like Chirp Dynamics Under Constrained Conditions

GR describes the chirp behavior through spacetime curvature and metric perturbations, while UMH describes the chirp through a wave-propagation formulation in which GR behavior appears as an effective large-scale description.

In the present implementation, UMH matches the observed chirp structure without invoking cosmological-expansion-based amplitude scaling or additional phenomenological corrections. The fact that the UMH waveform aligns with the GW150914 signal using a forward model and without PN orders beyond the leading dynamical behavior is consistent with the possibility that the observed waveform structure can arise from a forward-generated model without higher-order PN corrections.

The goal of this analysis is not to replace existing inference pipelines but to demonstrate that the GW150914 chirp can be forward-generated from a constrained forward model prior to comparison with detector data.

A physical medium couples frequency evolution, phase accumulation, and amplitude scaling through a single source–observer operator. In standard detector-frame waveform analyses, the redshift affecting the frequency and phase evolution is absorbed into the recovered detector-frame mass scale, while the source-frame interpretation of mass, distance, and redshift is assigned afterward through an assumed cosmological distance–redshift relation. The UMH calculation uses a different closure condition: the Pantheon+-calibrated operator (Z) is applied explicitly before comparison, so the source-frame configuration, observer-frame frequency evolution, phase accumulation, amplitude normalization, detector projection, and ringdown relaxation are determined together. The present result therefore does not show that standard template pipelines cannot recover GW150914; it shows that the UMH source–observer mapping can forward-generate the event under a fixed, coupled propagation constraint without template-bank search, frequency remapping, per-detector phase adjustment, or empirical amplitude fitting.

5.2.3 Physical Interpretation within the UMH Framework

General Relativity (GR) provides a highly successful mathematical description of gravitational radiation in terms of spacetime curvature and metric perturbations, but it does not posit a mechanical medium underlying wave propagation. The UMH framework models spacetime within a wave-propagation formulation in which a tensioned medium description is used in which oscillatory modes manifest as gravitational waves. In this view, GR describes the effective large-scale dynamics of gravitational radiation, while UMH provides a mechanistic interpretation of the processes underlying those dynamics.

Within the UMH picture, wave propagation speed, Lorentz invariance, energy loss from compact binaries, and ringdown relaxation are described within the UMH formulation through its wave-propagation dynamics. This interpretation remains consistent with the empirical successes of GW-pipelines while providing a framework for interpreting the origin of gravitational-wave signals. The same medium dynamics that generate binary-merger chirps also provide a unified mechanism connecting the gravitational-wave formulation to related cosmological applications.

More broadly, forward models that reproduce observed signals under a constrained set of model assumptions can provide strong predictive tests. In this context, the ability of the UMH framework to reproduce the observed GW150914 chirp structure without extensive parameter tuning highlights the ability of the UMH approach to reproduce observed signal structure under constrained assumptions.

5.3 Implications for Gravitational Physics

The results of this study are consistent with a medium-based interpretation of gravitational waves providing a framework for modeling waveform generation and propagation. Because the UMH model produces a waveform consistent with the observed GW150914 chirp structure without higher-order post-Newtonian corrections or phenomenological template tuning, it demonstrates a forward-model approach that may simplify aspects of waveform modeling, may reduce parameter degeneracies in future implementations, and offer different perspectives for interpreting compact binary mergers.

Because the UMH waveform is generated from explicit model dynamics rather than template interpolation, the framework provides a direct mapping between source parameters and waveform structure, suggesting that parameter inference may eventually be achievable within the same modeling framework.

6 Limitations and Scope

The primary objective is to establish that the UMH framework can forward-generate the observed chirp morphology prior to comparison with detector data.

The present analysis focuses on the large-scale morphology of the GW150914 waveform and does not examine potential small-scale residual structure in detail. The UMH framework allows for the possibility that additional small-scale features may arise from medium-level coherence effects or nonlinear interactions; however, a detailed investigation of such residual structure is beyond the scope of the present work.

Sky position, antenna orientation, and binary mass parameters were explored on a coarse diagnostic grid to identify the event configuration under the UMH source–observer mapping and to verify the stability of the generated chirp morphology. Because the present generator uses the leading-order 0PN-equivalent chirp evolution, the inspiral morphology is constrained primarily by the chirp mass M_c, while individual component masses and mass ratio are not claimed here as uniquely recovered source parameters. Full component-mass and spin inference within the UMH framework is deferred to future higher-order and event-level inference studies. The configuration shown corresponds to the strongest detector-network consistency point within this coarse event-configuration sweep, with nearby grid points producing slightly weaker but qualitatively similar matches. This sweep identifies the event-level source and geometry configuration; it does not reoptimize the Pantheon+-calibrated propagation mapping or introduce waveform-shape tuning, detector-specific phase adjustment, frequency remapping, empirical amplitude fitting, or waveform reparameterization during comparison. This work does not perform likelihood maximization or Bayesian parameter inference and is not intended to replace existing gravitational-wave inference pipelines. Its purpose is to demonstrate that the UMH forward model reproduces the observed waveform morphology once a physically consistent event configuration is specified. The agreement across both detectors emerges from the geometric projection once the global registration anchor is fixed and does not involve detector-specific adjustments. Full parameter inference within the UMH framework is deferred to future work.

Additionally, this work does not explore consistency across the full LIGO/Virgo event catalog. The goal of this paper is to demonstrate that UMH reproduces the core gravitational-wave phenomenology of GW150914 using only its fundamental mechanical principles. A comprehensive statistical analysis across multiple gravitational-wave events is deferred to future work.

The present analysis intentionally restricts the UMH waveform to a non-spinning, Newtonian-order configuration without extensive parameter sweeps or higher-order post-Newtonian refinements. The framework can in principle be extended to include intrinsic spin, broader parameter-space exploration, and multi-event population studies. These extensions are not required for the present morphology-level comparison and are therefore deferred to future work.

The present work therefore illustrates the baseline behavior of the UMH waveform model under minimal physical assumptions rather than presenting a fully optimized or extensively parameterized implementation.

7 Conclusions

The central result of this work is a cross-domain propagation test: the source–observer mapping calibrated entirely on Pantheon+ supernova data, fixed *a priori*, transfers unchanged to the gravitational-wave domain, where it consistently governs frequency evolution, phase accumulation, amplitude scaling, and time dilation with no event-specific adjustment.

The present analysis demonstrates that a gravitational-wave chirp consistent with the GW150914 event can be generated within the UMH forward model using Pantheon+ calibrated propagation. The resulting waveform reproduces the observed inspiral–merger–ringdown morphology, including frequency evolution, amplitude growth, merger timing, and ringdown behavior, using a forward model derived within the UMH framework.

For GW150914, the agreement with the LIGO observations is obtained using a single intrinsic UMH waveform projected onto the Hanford and Livingston detectors through standard antenna response functions and geometric time delays. The same constrained protocol is also applied to GW170814 using the Hanford, Livingston, and Virgo detector set. No per-detector parameter tuning, template-bank maximization, or phenomenological waveform adjustments are applied in the comparison.

The correspondence between the UMH prediction and the GW150914 signal is consistent with the essential structure of gravitational-wave chirps arising within the UMH formulation. This result illustrates that forward modeling within the UMH framework can reproduce the principal observational features of compact-binary mergers detected by LIGO.

These results indicate that a medium-based interpretation of gravitational waves provides a consistent framework for modeling waveform generation and propagation. Because the UMH model reproduces the observed chirp morphology using only leading-order orbital dynamics and without phenomenological template fitting, it demonstrates a forward-model approach that may simplify aspects of waveform modeling and provide perspectives for interpreting compact binary mergers.

Within the UMH framework, gravitational-wave dynamics are connected within the UMH framework to its cosmological formulations. If redshift, luminosity distance, and chirp evolution are described within the same formulation, then gravitational waves could serve as probes of the underlying model parameters. This raises the possibility that analyses of multiple gravitational-wave events could help constrain parameters of the UMH formulation, such as its effective tension or coupling parameters, potentially linking gravitational-wave observations with cosmological phenomena within the UMH framework.

Future work will extend this analysis to include higher-resolution parameter exploration, multi-event comparisons across the gravitational-wave catalog, and further investigation of potential medium-level signatures predicted by the UMH framework.

This study provides an observational consistency check for one prediction pathway of the ***UMH*** *Framework.*

A Pipeline Details

This appendix summarizes relevant implementation details for reproducibility.

A.1 UMH Chirp Generator Parameters

The UMH chirp generator (`UMH_Chirp_Generator.py`) produces:

- intrinsic strain $h_{\mathrm{UMH}}(t)$ for both polarizations,
- analytic frequency $f_{\mathrm{GW}}(t)$,
- merger and ringdown metadata,
- medium-tension redshift factors,
- binary parameters (masses, separation, chirp mass),
- soliton-grid options (disabled for this study).

The generator does **NOT**:

- access LIGO data,
- enable PN terms > 0,
- apply template fitting or time stretching,
- include expansion-based redshift corrections.

A.2 Detector Projection

The UMH intrinsic waveform is projected onto the active detector set for each event. For GW150914 this is Hanford and Livingston; for GW170814 this includes Hanford, Livingston, and Virgo via:

$h_D(t) = F_D^{+}(\theta, \phi, \psi)\, h_{+}(t - \Delta t_D) + F_D^{\times}(\theta, \phi, \psi)\, h_{\times}(t - \Delta t_D)$, equation (36),

where $F_D^{+,\times}$ are antenna pattern functions and Δt_D is the geometric delay.

A single fixed UMH medium-tension parameter is used to define the source–observer mapping, which consistently determines gravitational-wave time dilation, frequency evolution, phase accumulation, and amplitude–distance scaling. No per-detector normalization, phase adjustment, or empirical tuning is performed. The UMH–LIGO agreement is obtained using non-spinning UMH binaries and a single ASD-based whitening step, whereas GW-pipeline based waveform templates typically employ template-bank–based matched filtering together with calibration marginalization and parameter-space maximization.

A.3 LIGO Processing Parameters

LIGO strain data (16384 Hz sampling) are processed with:

- Tukey window,
- dynamically determined bandpass filtering (20–287.32 Hz for the GW150914 run shown; the GW170814 secondary-event run uses its own generator-derived upper band edge),
- whitening via ASD estimate,
- Hilbert transform for instantaneous frequency,
- 4096-sample spectrogram windows with 50% overlap.

A.4 Comparison Compiler Outputs

The comparison pipeline (`UMH_Ligo_Compiler.py`) produces:

- correlation windows and whitened overlaps,
- ASD comparison curves,
- dual spectrograms (UMH vs LIGO),
- instantaneous frequency mismatch,
- SNR estimates and detector-response diagnostics,
- full JSON summaries of all diagnostic metrics.

The comparison compiler is strictly independent of the generator.

B Numerical Validation

B.1 Residual Behavior

Residuals between the UMH waveform and whitened LIGO data remain consistent with instrument noise for both detectors. Hanford shows a particularly clean match; Livingston exhibits higher broadband noise, consistent with known GW150914 characteristics.

B.2 Convergence and Stability

The numerical evolution of the intrinsic UMH chirp is stable across:

- timestep variations,
- small perturbations in binary parameters,
- different whitening windows,
- different ASD estimates.

UMH instantaneous frequency remains consistent under all tested configurations.

B.3 Diagnostic Checks

Diagnostic outputs include:

- Network SNR consistency.
- Residual noise inflation,
- Windowed correlation,
- Frequency-mismatch values,
- Maximum and median strain ratios,
- Normalized correlation window maxima,

These diagnostics demonstrate that the UMH chirp closely reproduces the GW150914 morphology under fixed, physically constrained registration conditions without waveform-level tuning.

B.4 Pantheon+ Calibration and Model Comparison

The purpose of this appendix is to document the external calibration used by the present gravitational-wave analysis, not to repeat the information-criterion argument of the companion Pantheon+ study. The model-comparison and parameter-counting conventions are discussed in Ref. [2]. In the present paper, the Pantheon+-calibrated coefficients are treated only as fixed external inputs to the gravitational-wave generator and are not adjusted using GW150914 or GW170814 data.

Table 10: Pantheon+-calibrated quantities imported into the gravitational-wave generator.

Quantity	**Role in GW generator**	**Origin**	**Treatment here**
α	Geometric source–observer redshift scale $D_{\mathrm{geom}}(z) = \ln(1+z)/\alpha$	Pantheon+ calibration	Fixed external input
β_1, β_2	Transmission/relaxation coefficients entering $T(z)$ and $\beta_{\mathrm{eff}}(z)$	Pantheon+ calibration	Fixed external inputs
δ	Time-dilation exponent used in D_L^{UMH}	UMH Lorentz-invariant prediction	Fixed, $\delta = 1$
D_L^{UMH}	Event-level effective luminosity-distance input	Source configuration using the UMH mapping	Fixed per event

The gravitational-wave test performed here depends only on the fact that these quantities are fixed before comparison with detector strain. The UMH redshift relation used by the generator is therefore not a ΛCDM luminosity-distance integral; it is the source–observer mapping defined by Eqs. 20–24. The transmission coefficients β_1 and β_2 do enter the effective luminosity-distance and relaxation mappings, but they are not recalibrated or varied in the gravitational-wave analysis. Consequently, the present GW150914 result is independent of the parameter-counting convention adopted for the Pantheon+ information-criterion comparison.

B.5 UMH ringdown damping and frequency-relaxation quantities

Table 11: UMH ringdown damping and frequency-relaxation quantities used in the reported event runs.

Event	$f_{\mathrm{RD,src}}$ Hz	$f_{\mathrm{RD,obs}}$ Hz	$\tau_{\mathrm{RD,src}}$ ms	$\tau_{\mathrm{RD,obs}}$ ms	β_{eff}	$\tau_{\mathrm{relax,obs}}$ ms
GW150914	248.024	229.855	4.032	4.351	0.4116	1.791
GW170814	225.725	202.224	4.430	4.945	0.3933	1.945

The damping time is fixed in the source frame by $\tau_{\mathrm{RD,src}} = N_{\mathrm{RD}}/f_{\mathrm{RD,src}}$ with $N_{\mathrm{RD}} = 1.00$. The amplitude envelope decays on $\tau_{\mathrm{UMH}} \equiv \tau_{\mathrm{RD}}$, while the frequency retunes on the transport-modified timescale $\tau_{\mathrm{relax}} = \beta_{\mathrm{eff}}\tau_{\mathrm{RD}}$. Observer-frame times are obtained by multiplying source-frame times by $Z = 1 + z_{\mathrm{UMH}}$.

C Polarization Structure and the Spin-2 Character of the Radiation

A natural question is how the two transverse–traceless (TT) polarizations characteristic of spin-2 gravitational radiation arise within a formulation whose linearized wave equation (Eq. 41) is written for a scalar amplitude Ψ. The resolution is that Ψ is used here as the scalar *amplitude coordinate* of a medium displacement mode, not as a fundamental spin-0 radiative field by itself. The scalar wave equation governs the propagation of the mode amplitude; the detector-coupled radiative observable is the transverse–traceless strain tensor associated with the underlying displacement structure of the medium. Thus, acceptance of the radiation normalization used here rests on the recovered TT far-field construction of Ref. [1]; the present paper tests the propagation and detector-frame consequences of that sector rather than rederiving it.

In the far-field radiative sector used by the present gravitational-wave generator, the observable strain is therefore represented by the TT tensor h_{ij}^{TT}. The full finite-strain and covariant construction, in which curvature and the effective metric arise from the medium displacement structure, is given in Ref. [1]. The present paper does not attempt to rederive the complete spin-2 construction from the scalar amplitude equation alone; instead, it uses the recovered far-field TT sector of the UMH framework, consistent with the GR-limit quadrupole radiation law used in Secs. 2.3–2.5.

For a wave propagating along the local $\hat{z}$ direction, the two detector-frame TT polarizations are defined in the usual way by

$$h_+(t) = \tfrac{1}{2}\left[\, h_{xx}^{\mathrm{TT}}(t) - h_{yy}^{\mathrm{TT}}(t) \,\right], \qquad h_\times(t) = h_{xy}^{\mathrm{TT}}(t). \tag{39}$$

These are the quantities subsequently projected onto each detector through the antenna response functions F_D^+ and $F_D^\times$ in Eq. 36. The antenna functions therefore project the TT strain already supplied by the radiative sector of the medium dynamics; they do not supply the tensor character themselves.

The leading-order amplitude of this TT strain reproduces the standard quadrupole result in the effective GR limit. For an outgoing far-field disturbance, matching the mechanical energy flux of the radiating displacement mode, with time-averaged scaling $\langle S\rangle \sim T_u\, c\, \langle(\nabla\Psi)^2\rangle$ integrated over a sphere, to the gravitational-wave luminosity fixes the radiative normalization. This yields the far-field TT amplitude with the familiar $2G/c^4$ prefactor and $1/r$ falloff, recovering the leading-order GR quadrupole amplitude. Consistent with the emergence of the GR limit established for the chirp evolution, the spin-2 quadrupolar amplitude is therefore treated here as a recovered far-field sector of the UMH dynamics rather than as an independently fitted input. A complete derivation from the mechanical-emission side is provided in Ref. [1].

Absence of an additional radiative polarization. Although the medium may support both transverse and longitudinal disturbances at the substrate level, the forward-generated waveform used in this paper is restricted to the far-field transverse–traceless radiative sector that enters the detector response. Longitudinal and trace-like medium responses are not included as propagating detector-frame polarizations in the present comparison. The waveform therefore carries only the two TT polarizations h_+ and $h_\times$, consistent with the two-polarization tensor response used in the present LIGO comparison. A detailed treatment of the radiative content of the medium modes is given in Ref. [1].

D UMH Theory

This appendix summarizes the mathematical formulation underlying the propagation model used in the present analysis. It is included for completeness and is not required for interpretation of the main results.

The Ultronic Medium Hypothesis (UMH) proposes a mechanical framework in which General Relativity (GR) and Quantum Field Theory are recovered as effective large-scale descriptions within a tension-based wave formulation. In this representation, gravitational waves are described as coherent strain-like disturbances within the UMH model, with the familiar metric description of GR corresponding to an effective macroscopic representation of these dynamics.

This study addresses prediction via forward physical generation rather than inverse waveform fitting and does not replace the GR description of gravitational waves, but instead investigates whether the UMH formulation can generate the same observable chirp morphology under a constrained physical model. Because gravitational waves propagate across hundreds of megaparsecs before detection, events such as GW150914 provide a natural cosmological-scale test of the propagation behavior described within this framework.

The complete UMH framework formulates relativistic propagation, gravitational curvature, and cosmological dynamics within a wave-based representation described in Ref. [1]. The present work focuses on a single observational consequence of this formulation: the generation and propagation of gravitational-wave chirps.

Within the UMH formulation, spacetime is represented as a continuous tension-based medium described by a scalar displacement field $\Psi(\mathbf{x}, t)$. In the linear regime, the field obeys a relativistic wave equation characterized by effective tension T_u and density ρ_u. Here the *linear regime* denotes small-amplitude perturbations for which the nonlinear potential $V(\Psi)$ in Eq. (42) contributes negligibly, so the field obeys the linear wave equation Eq. (41) with propagation speed set by Eq. (40).

The propagation speed in the UMH formulation is determined by the ratio of tension to density:

$$c = \sqrt{\frac{T_u}{\rho_u}} \tag{40}$$

which is consistent with Lorentz-invariant propagation without introducing a preferred frame, and is consistent with the emergence of GR-like behavior as an effective macroscopic description. Here ρ_u denotes the effective mechanical density parameter of the UMH medium entering the wave-speed relation; it is not the cosmological constant, not Ω_Λ, and not a vacuum-energy density in the ΛCDM sense.

In the linear small-amplitude limit, the medium displacement field therefore obeys the standard tension–density wave equation,

$$\rho_u \frac{\partial^2 \Psi}{\partial t^2} - T_u \nabla^2 \Psi = 0, \tag{41}$$

which has the characteristic propagation speed $c = \sqrt{T_u/\rho_u}$ used throughout the waveform generation. The field dynamics in this formulation are described by the Lagrangian density

$$\mathcal{L} = \frac{1}{2}\rho_u(\partial_t \Psi)^2 - \frac{1}{2}T_u(\nabla\Psi)^2 - V(\Psi), \tag{42}$$

from which the nonlinear evolution equation $\rho_u \partial_t^2 \Psi - T_u \nabla^2 \Psi + \partial V/\partial\Psi = 0$ is obtained through the action principle $S = \int \mathcal{L}\, d^3x\, dt$.

The associated wave-energy density:

$$U = \frac{1}{2}\rho_u \left(\frac{\partial \Psi}{\partial t}\right)^2 + \frac{1}{2}T_u \left(\nabla\Psi\right)^2 \tag{43}$$

describes energy transport within the UMH formulation and provides a mechanism by which binary orbital energy can be represented as propagating disturbances.

In the far-field limit the observable gravitational-wave strain $h(t)$ is proportional to the transverse propagating perturbation of the UMH field Ψ projected through the detector response. A complete derivation of the UMH formulation, including its covariant structure and effective field equations, is presented in [1]. The field formulation is constructed to respect standard conservation laws through the Noether currents associated with time and spatial translation symmetry. These properties are consistent with energy and momentum transport following the same conservation principles used in gravitational-wave radiation analyses.

In this framework, the behavior of compact binaries — orbital decay, chirp formation, and ringdown — is described as arising from energy transfer into the field and the resulting strain propagation, with the geometric spacetime description of GR corresponding to an effective macroscopic representation of these processes.

This perspective allows gravitational-wave signals to be modeled within a forward physical framework based on the UMH formulation, without requiring phenomenological template families[8] or detector-specific calibration terms.

The comparison is performed under a strictly constrained procedure: one intrinsic UMH waveform, one cosmologically calibrated propagation parameter, and one global registration anchor. No per-detector tuning, phase adjustment, frequency remapping, amplitude fitting, or template optimization is applied during the comparison, and the intrinsic waveform is generated independently of the LIGO strain data.

Previous UMH work has shown that tension-driven energy exchange is consistent with cosmological redshift, luminosity–distance relations, and time-dilation scaling within the same formulation [2]. In that analysis, the propagation parameter governing the source–observer mapping (equivalently an effective tension scale within the model) is fixed using the Pantheon+ Type Ia supernova dataset.

The present work adopts that same calibration without modification in the gravitational-wave domain, allowing GW150914 to serve as an independent cross-domain test of the UMH propagation law. While cosmology is not the focus of this paper, this prior result is consistent with the UMH formulation providing a unified description across multiple observational domains under a single parameterization.

The UMH propagation parameter governing the source–observer mapping is fixed by the Pantheon+ Type Ia supernova calibration, yielding $\alpha = (2.48 \pm 0.08) \times 10^{-4}\,\mathrm{Mpc}^{-1}$ [2], and is not recalibrated for gravitational-wave observations.

Here we apply the UMH formulation in the gravitational-wave regime by asking whether its dynamical structure is consistent with reproducing the observed features of the GW150914 [6] event. Rather than adopting the post-Newtonian (PN) [7] expansions or phenomenological template families typically used in gravitational-wave pipelines, we evaluate a strictly constrained forward prediction within the UMH formulation using an independent chirp generator and an equally independent comparison pipeline.

This constitutes a direct observational test of the UMH formulation in the strong-gravity, high-frequency regime and establishes gravitational-wave observations as an independent probe of the model.

The full UMH framework, including its field equations, Lorentz-invariant wave-speed construction within the formulation, curvature mapping, and gauge-theoretic extensions, is presented in ref. [1]; the present paper restricts attention to one observable consequence of that framework, namely forward gravitational-wave chirp generation.

The present work does not attempt to re-derive the full UMH framework. Instead, it tests a specific observable consequence of the theory: whether the dynamical formulation yields gravitational-wave chirps consistent with the GW150914 signal when the UMH propagation law is fixed by independent cosmological calibration and no event-specific waveform tuning is introduced.

D.1 Background

The UMH formulation has previously been shown to be consistent with cosmological redshift, luminosity–distance relations, and time-dilation behavior in the Pantheon+ Type Ia supernova sample [3, 4]. These results are obtained using a single propagation parameter calibrated from cosmological data [2], which is applied unchanged in the present gravitational-wave analysis.

This provides the basis for evaluating whether a single propagation mapping can consistently describe both cosmological observations and gravitational-wave signals such as GW150914.

E Key Equations from UMH Theory

The Ultronic Medium Hypothesis (UMH) describes gravitational radiation within a wave-based formulation as propagating strain-like disturbances governed by a tension–density relation. The following equations summarize the core mathematical relations used in this analysis.

Energy Power Form 1

$$\frac{dE}{dt} = -\oint \mathbf{F}_\Psi \cdot d\mathbf{A},$$

This relation expresses conservation of energy for the wave field, where the change in total energy equals the net outward flux of wave energy $\mathbf{F}_\Psi$ *through a closed surface. It describes how energy carried by propagating disturbances leaves the source region.*

Energy-loss law: Equation 2

$$\frac{dE}{dt} = -\mathcal{P}_{\rm GW}(t),$$

Expresses the rate at which the binary's orbital energy decreases due to gravitational-wave power radiated by the system. Here $\mathcal{P}_{\rm GW}$ *denotes the radiated gravitational-wave energy flux associated with the propagating strain field.*

Frequency-evolution relation: Equation 3

$$\frac{d\Omega}{dt} = -\frac{\mathcal{P}_{\rm GW}}{dE/d\Omega},$$

Links the chirp rate $d\Omega/dt$ *to the ratio of GW power to the derivative of orbital energy, forming the core dynamical equation for inspiral hardening. Where* $\mathcal{P}_{\rm GW}$ *is the mechanical strain-energy flux radiated by the binary.*

Newtonian orbital energy frequency: Equation 4

$$E(\Omega) \propto -\,\Omega^{2/3},$$

This relation expresses the Newtonian scaling between a binary system's orbital energy and orbital frequency, showing that the binding energy becomes more negative as the inspiral frequency increases.

Leading-order chirp: Equation 5

$$\frac{d\Omega}{dt} \propto \Omega^{11/3},$$

Gives the Newtonian (0PN) power-law scaling $d\Omega/dt \propto \Omega^{11/3}$*, showing the characteristic accelerating inspiral.*

Newtonian Orbital Energy: Equation 6

$$E_{\rm orb} = -\frac{Gm_1m_2}{2r}.$$

This equation gives the Newtonian gravitational binding energy of a two-body binary system in a circular orbit, showing how the orbital energy depends on the component masses and their separation.

Chirp Radiation Power: Equation 7

$$P_{\rm rad} = \frac{32}{5}\frac{G^{7/3}}{c^5}M_c^{10/3}(\pi f)^{10/3},$$

This equation gives the leading-order power radiated as gravitational waves from a compact binary system as a function of its chirp mass and orbital frequency.

Orbital Energy Balance: Equation 8

$$\frac{dE_{\rm orb}}{dt} = -P_{\rm rad}.$$

This equation expresses energy conservation in a radiating binary system, stating that the loss of orbital binding energy equals the power carried away by gravitational radiation.

Kepler Orbital Relation: Equation 9

$$\Omega^2 = \frac{G(m_1+m_2)}{r^3}$$

This equation is Kepler's relation for a binary system, linking the orbital angular frequency to the total mass of the system and the orbital separation.

Frequency Relation: Equation 10

$$f = \frac{\Omega}{\pi},$$

This relation states that the gravitational-wave frequency is twice the orbital frequency of the binary system.

Leading Order Chirp Evolution: Equation 11

$$\frac{df}{dt} = \frac{96}{5}\pi^{8/3}\left(\frac{GM_c}{c^3}\right)^{5/3} f^{11/3},$$

This equation gives the leading-order (0PN) evolution of the gravitational-wave frequency during binary inspiral, showing how the chirp accelerates as orbital energy is radiated away.

UMH strain-amplitude: Equation 12

$$h(t) = \frac{A_*}{D_L^{\rm UMH}}\,\mathcal{S}(t),$$

Defines the detector-independent strain amplitude in terms of the intrinsic source amplitude scale A_**, the intrinsic UMH strain function* $\mathcal{S}(t)$*, and the UMH effective luminosity distance* $D_L^{\rm UMH}$*. The source–observer redshift, time-dilation, and transmission factors enter through* $D_L^{\rm UMH}$*, so they are not applied again as a separate multiplicative factor in this equation.*

UMH Low-z Calibration: Equation 13

$$L \equiv \ln(1+z) \simeq \alpha D_{\rm geom}.$$

Defines the low-redshift UMH geometric-distance calibration used in the Pantheon+ analysis to fix the propagation scale α *independently of the gravitational-wave data. Here* $D_{\rm geom}$ *is the geometric source–observer distance, distinct from the UMH effective luminosity distance* $D_L^{\rm UMH}$ *used as the event-distance input.*

Gravitational-wave frequency: Equation 14

$$f_{\rm GW}(t) = \frac{\Omega(t)}{\pi},$$

Relates the GW frequency to the orbital angular frequency via $f_{\rm GW} = \Omega/\pi$*.*

Phase-evolution integral: Equation 15

$$\phi(t) = \phi_0 + 2\pi\int_{t_0}^{t} f_{\rm GW}(t')\,dt'.$$

Constructs the waveform phase by integrating the instantaneous GW frequency over time.

UMH Newtonian chirp evolution: Equation 16

$$\frac{df_{\rm GW}}{dt} = K_{\rm UMH}\,f_{\rm GW}^{11/3},$$

Defines the Newtonian-order differential evolution of the gravitational-wave frequency in UMH, describing mechanical orbital hardening through medium-mediated energy transfer. This evolution law integrates to the standard analytic chirp scaling $f_{\rm GW}(t) \propto (t_c - t)^{-3/8}$ *without invoking post-Newtonian expansions, phenomenological fitting, or adjustable shape parameters.*

Chirp Mass: Equation 17

$$M_c = \frac{(m_1 m_2)^{3/5}}{(m_1 + m_2)^{1/5}}.$$

This relation defines the binary chirp mass, the effective mass parameter governing the inspiral frequency evolution of gravitational-wave emission.

UMH Chirp Coefficient: Equation 18

$$K_{\mathrm{UMH}} = \frac{96}{5}\,\pi^{8/3}\left(\frac{G\,M_{c,\mathrm{src}}}{c^3}\right)^{5/3}.$$

This relation defines the chirp coefficient K_{UMH}*, which determines the leading-order inspiral frequency evolution from the binary's chirp mass.*

UMH Newtonian chirp solution: Equation 19

$$t_c - t = \frac{3}{8K_{\mathrm{UMH}}}\,f_{\mathrm{GW}}^{-8/3}, \qquad f_{\mathrm{GW}}(t) \propto (t_c - t)^{-3/8}.$$

Gives the closed-form analytic solution of the UMH Newtonian chirp evolution, relating gravitational-wave frequency to time-to-coalescence. This expression captures the characteristic rising-frequency inspiral behavior observed in compact binary mergers without invoking post-Newtonian expansions, phenomenological fitting, or adjustable shape parameters.

UMH redshift mapping: Equation 20

$$z_{\mathrm{UMH}} = z_{\mathrm{UMH}}(D_{\mathrm{geom}}; \alpha)$$

Defines the UMH tension redshift as a function of geometric source–observer distance and the Pantheon+-calibrated propagation scale.

UMH geometric distance: Equation 21

$$D_{\mathrm{geom}}(z) = \frac{\ln(1+z)}{\alpha}$$

Defines the homogeneous-limit geometric distance corresponding to a given UMH redshift.

UMH source–observer factor: Equation 22

$$Z \equiv 1 + z_{\mathrm{UMH}}$$

Defines the source–observer redshift factor used to map source-frame quantities to observer-frame quantities.

UMH transmission factor: Equation 23

$$T(z) = \exp\Big[-\beta_1 \ln(1+z) - \beta_2 \ln^2(1+z)\Big]$$

Defines the Pantheon+-calibrated broadband transmission factor entering the UMH luminosity-distance mapping.

UMH effective luminosity distance: Equation 24

$$D_L^{\mathrm{UMH}}(z) = D_{\mathrm{geom}}(z)(1+z)^{(1+\delta)/2}T(z)^{-1/2}, \qquad \delta = 1$$

Defines the UMH effective luminosity distance used for amplitude normalization and event-level source-distance inputs.

UMH effective relaxation coefficient: Equation 25

$$\beta_{\mathrm{eff}}(z_{\mathrm{UMH}}) = \beta_1 + 2\beta_2 \ln(1 + z_{\mathrm{UMH}})$$

Defines the local transport coefficient used for post-merger frequency relaxation.

UMH frequency redshift: Equation 26

$$f_{\mathrm{obs}}(t) = Z^{-1} f_{\mathrm{src}}(t)$$

Maps the source-frame gravitational-wave frequency to the observer-frame frequency through the UMH source–observer factor.

UMH observer-frame phase: Equation 27

$$\phi_{\mathrm{obs}}(t) = \phi_0 + 2\pi \int_{t_0}^{t} f_{\mathrm{obs}}(t')\,dt'$$

Defines the observed phase accumulation after applying the UMH frequency-redshift mapping.

UMH reference amplitude normalization: Equation 28

$$h_{\mathrm{ref}}^{\mathrm{UMH}} = \frac{4G^{5/3} M_{c,\mathrm{src}}^{5/3}\,(\pi f_{\mathrm{ref,src}})^{2/3}}{c^4 D_L^{\mathrm{UMH}}}, \qquad f_{\mathrm{ref,src}} = Z f_{\mathrm{ref,obs}}$$

Defines the single global strain-amplitude normalization used by the generator.

UMH detector strain projection: Equation 29

$$h_d(t) = F_{+,d} A_{\mathrm{obs}}(t-\tau_d)\,\frac{1+\cos^2\iota}{2}\,\cos[\phi_{\mathrm{obs}}(t-\tau_d)] + F_{\times,d} A_{\mathrm{obs}}(t-\tau_d)\cos\iota\,\sin[\phi_{\mathrm{obs}}(t-\tau_d)]$$

Defines the detector-frame strain after antenna projection, inclination projection, phase evolution, and geometric delay.

UMH ringdown model: Equation 30

$$h_{\mathrm{RD}}(t) = A_{\mathrm{RD}}\, e^{-(t-t_m)/\tau_{\mathrm{UMH}}}\,\sin[\phi_{\mathrm{RD}}(t)], \qquad t \geq t_m, \qquad \frac{d\phi_{\mathrm{RD}}}{dt} = 2\pi f(t).$$

Represents the post-merger signal as a damped UMH relaxation response whose amplitude decays on the intrinsic medium timescale while the phase is generated by the instantaneous post-merger frequency $f(t)$*, which relaxes toward the asymptotic ringdown frequency* f_{RD}*.*

GR-limit $(2, 2, 0)$ **Reference Scale: Equation 31**

$$f_{220,\mathrm{src}} = \frac{c^3}{2\pi G M_f}\left[1.5251 - 1.1568(1-a_f)^{0.1292}\right], \qquad f_{220,\mathrm{obs}} = \frac{f_{220,\mathrm{src}}}{1+z_{\mathrm{UMH}}},$$

Represents the GR-limit $(2, 2, 0)$ *ringdown reference frequency and observer-frame redshift mapping.*

UMH Ringdown Relaxation: Equation 32

$$\tau_{\mathrm{relax}} = \beta_{\mathrm{eff}}\,\tau_{RD},$$

This equation relates the effective post-merger relaxation timescale of this model to the intrinsic ringdown damping time through the medium transport parameter.

Tau Identification: Equation 33

$$\tau_{\mathrm{UMH}} \equiv \tau_{RD}.$$

This relation identifies the UMH medium damping time with the intrinsic ringdown timescale governing the post-merger relaxation dynamics.

UMH Postmerger Frequency: Equation 34

$$f(t) = f_{RD} - (f_{RD} - f_{\text{merge}}) \exp\left[-\frac{t - t_m}{\tau_{\text{relax}}}\right], \qquad t \geq t_m,$$

This equation describes the post-merger frequency evolution as an exponential relaxation of the instantaneous frequency from the merger value toward the asymptotic ringdown frequency governed by the medium relaxation timescale.

UMH Merger Condition: Equation 35

$$\left.\frac{f}{df/dt}\right|_{f=f_{\text{merge}}} \simeq \tau_{RD}.$$

This condition defines the merger transition as the point where the inspiral frequency-evolution timescale becomes comparable to the intrinsic ringdown damping timescale of the system.

Detector response projection: Equation 36

$$h_D(t) = F_D^{+}(\theta, \phi, \psi)\, h_+(t - \Delta t_D) + F_D^{\times}(\theta, \phi, \psi)\, h_\times(t - \Delta t_D),$$

Converts the plus and cross polarizations into the strain seen by a specific detector using its antenna pattern and geometric time delay.

Hilbert instantaneous-frequency estimator: Equation 37

$$f_{\text{Hilbert}}(t) = \frac{1}{2\pi} \frac{d}{dt} \left[\arg(h(t) + i\, \mathcal{H}[h(t)])\right],$$

Derives the detector-frame instantaneous frequency from the analytic signal formed via the Hilbert transform.

UMH LIGO Correlation: Equation 38

$$r = \frac{\sum_i (h_{\text{UMH},i} - \bar{h}_{\text{UMH}})(h_{\text{LIGO},i} - \bar{h}_{\text{LIGO}})}{\sigma_{\text{UMH}} \sigma_{\text{LIGO}}},$$

Where r is the Pearson correlation coefficient between the UMH waveform and the LIGO strain time series.

Defines the plus and cross polarization components: Equation 39

$$h_+(t) = \tfrac{1}{2}\left[\, h_{xx}^{\text{TT}}(t) - h_{yy}^{\text{TT}}(t) \,\right], \qquad h_\times(t) = h_{xy}^{\text{TT}}(t).$$

Defines the two transverse–traceless polarization components extracted from the strain tensor: the plus mode h_+ as the difference of the diagonal strain components and the cross mode $h_\times$ as the off-diagonal component. These are the two detector-coupled TT radiative degrees of freedom in the plane orthogonal to propagation, and they constitute the polarizations projected onto each detector through the antenna response functions.

Wave Propagation Speed: Equation 40

$$c = \sqrt{\frac{T_u}{\rho_u}}$$

Wave propagation speed in a medium, derived from tension and mass density.

Wave Equation in a Medium 41

$$\rho_u \frac{\partial^2 \Psi}{\partial t^2} - T_u \nabla^2 \Psi = 0,$$

This relation is the governing wave equation for perturbations in the model medium, describing the propagation of strain disturbances with wave speed $c = \sqrt{\frac{T_u}{\rho_u}}$.

Wave Function Lagrangian 42

$$\mathcal{L} = \frac{1}{2}\rho_u (\partial_t \Psi)^2 - \frac{1}{2} T_u (\nabla \Psi)^2 - V(\Psi),$$

Lagrangian for a scalar field including kinetic, spatial gradient (tension), and potential energy terms.

Wave Energy Density 43

$$U = \frac{1}{2}\rho_u \left(\frac{\partial \Psi}{\partial t}\right)^2 + \frac{1}{2} T_u \,(\nabla \Psi)^2$$

Total energy of a wave field with kinetic and potential components integrated over volume.

F Data and Code Availability

All simulation and analysis code used in this study, including `UMH_Chirp_Generator.py`, `UMH_Ligo_Compiler.py`, and associated data processing scripts, are publicly available at the official UMH repository:

`https://github.com/UltronicPhysics/UMH`.

A versioned archive of the corresponding release is preserved on Zenodo and can be cited via DOI: 10.5281/zenodo.16651832. The repository includes simulation configuration files, output data, and figures used to produce the results in this paper.

References

[1] Dodge, A. (2025). The Ultronic Medium Hypothesis (UMH): A Mechanical Foundation Wave-Based Model of Reality. Framework. Zenodo. https://doi.org/10.5281/zenodo.17497461

[2] Dodge, A. (2025). Pantheon+ and Redshift Validation of the Ultronic Medium Hypothesis (UMH). Zenodo. https://doi.org/10.5281/zenodo.17860437

[3] Scolnic, D., Brout, D., Carr, A., et al. (2022). The Pantheon+ Analysis: The Full Data Set and Light-curve Release. *The Astrophysical Journal*, **938**(2), 113. https://doi.org/10.3847/1538-4357/ac8b7a

[4] Brout, D., Scolnic, D., Popovic, B., *et al.* (2022). The Pantheon+ Analysis: Cosmological Constraints. *The Astrophysical Journal*, **938**(2), 110. https://doi.org/10.3847/1538-4357/ac8e04

[5] Vallisneri, M., Kanner, J., Williams, R., Weinstein, A., & Stephens, B. (2015). The LIGO Open Science Center. *Journal of Physics: Conference Series*, **610**(1), 012021. https://doi.org/10.1088/1742-6596/610/1/012021

[6] Abbott, B. P., Abbott, R., Abbott, T. D., *et al.* (2016). Observation of Gravitational Waves from a Binary Black Hole Merger. *Physical Review Letters*, **116**(6), 061102. https://doi.org/10.1103/PhysRevLett.116.061102

[7] Blanchet, L. (2014). Gravitational Radiation from Post-Newtonian Sources and Inspiralling Compact Binaries. *Living Reviews in Relativity*, **17**, 2. https://doi.org/10.12942/lrr-2014-2

[8] Buonanno, A., & Damour, T. (1999). Effective One-Body Approach to General Relativistic Two-Body Dynamics. *Physical Review D*, **59**, 084006. https://doi.org/10.1103/PhysRevD.59.084006

[9] Blackman, J., Field, S. E., Scheel, M. A., et al. (2017). A Surrogate Model of Spinning Binary Black Hole Mergers. *Physical Review D*, **95**(10), 104023. https://doi.org/10.1103/PhysRevD.95.104023

[10] Boashash, B. (1992). Estimating and Interpreting the Instantaneous Frequency of a Signal — Part 1: Fundamentals. *Proceedings of the IEEE*, **80**(4), 520–538. https://doi.org/10.1109/5.135376

[11] Cohen, L. (1995). *Time–Frequency Analysis*. Englewood Cliffs, NJ: Prentice Hall PTR. ISBN 0-13-594532-1. https://www.worldcat.org/oclc/31516509

[12] Abbott, B. P., Abbott, R., Abbott, T. D., et al. (LIGO Scientific Collaboration and Virgo Collaboration) (2016). GW150914: First Results from the Search for Binary Black Hole Coalescence with Advanced LIGO. *Physical Review D*, **93**(12), 122003. https://doi.org/10.1103/PhysRevD.93.122003

[13] Abbott, B. P., Abbott, R., Abbott, T. D., et al. (LIGO Scientific Collaboration and Virgo Collaboration) (2016). Observing Gravitational-Wave Transient GW150914 with Minimal Assumptions. *Physical Review D*, **93**(12), 122004. https://doi.org/10.1103/PhysRevD.93.122004

[14] Abbott, B. P., Abbott, R., Abbott, T. D., et al. (LIGO Scientific Collaboration and Virgo Collaboration) (2017). GW170814: A Three-Detector Observation of Gravitational Waves from a Binary Black Hole Coalescence. *Physical Review Letters*, **119**(14), 141101. https://doi.org/10.1103/PhysRevLett.119.141101

[15] Allen, B. (2005). A χ^2 time–frequency discriminator for gravitational wave detection. *Physical Review D*, 71(6), 062001. doi:10.1103/PhysRevD.71.062001

[16] Tukey, J. W. (1967). An introduction to the calculations of spectra. In B. Harris (Ed.), *Spectral Analysis of Time Series* (pp. 25–46). New York: Wiley.